IOP Publishing Plasma Sources Science and Technology

Plasma Sources Sci. Technol. **24** (2015) 035026 (24pp) doi:10.1088/0963-0252/24/3/035026

Formation of reactive oxygen and nitrogen species by repetitive negatively pulsed helium atmospheric pressure plasma jets propagating into humid air

Seth A Norberg[1], Eric Johnsen[1] and Mark J Kushner[2,3]

[1] Department of Mechanical Engineering, University of Michigan, 2350 Hayward Street, Ann Arbor, MI 48109-2125, USA
[2] Department of Electrical Engineering and Computer Science, University of Michigan, 1301 Beal Avenue, Ann Arbor, MI 48109-2122, USA

E-mail: norbergs@umich.edu, ejohnsen@umich.edu, mjkush@umich.edu

Received 4 March 2015, revised 13 April 2015
Accepted for publication 27 April 2015
Published 8 June 2015

Abstract

Atmospheric pressure plasma jets have many beneficial effects in their use in surface treatment and, in particular, plasma medicine. One of these benefits is the controlled production of reactive oxygen and nitrogen species (RONS) in the active discharge through the molecular gases added to the primary noble gas in the input mixture, and through the interaction of reactive species in the plasma effluent with the ambient air. In this computational investigation, a parametric study was performed on the production of RONS in a multiply pulsed atmospheric pressure plasma jet sustained in a He/O_2 mixture and flowing into ambient humid air. The consequences of flow rate, O_2 fraction, voltage, and repetition rate on reactant densities after a single discharge pulse, after 30 pulses, and after the same total elapsed time were investigated. At the end of the first discharge pulse, voltage has the greatest influence on RONS production. However, the systematic trends for production of RONS depend on repetition rate and flow rate in large part due to the residence time of RONS in the plasma zone. Short residence times result in reactive species produced by the previous pulse still being in the discharge tube or in the path of the ionization wave at the next pulse. The RONS therefore accumulate in the tube and in the near effluent on a pulse-to-pulse basis. This accumulation enables species requiring multiple reactions among the primary RONS species to be produced in greater numbers.

Keywords: plasma jet, atmospheric pressure plasma, humid air, repetitive pulsing, RONS (reactive oxygen nitrogen species), model

(Some figures may appear in colour only in the online journal)

I. Introduction

Non-equilibrium atmospheric pressure plasma jets (APPJs) provide therapeutic and sterilizing effects in the context of biomedical treatment of surfaces through delivery of fluxes of photons, charged and reactive species, and electric fields to tissue [1–5]. Although the devices are geometrically simple, the structure of the plasma in APPJs can be quite complex, as demonstrated by early observations of *plasma bullets* propagating through the plume of an APPJ. This complexity has motivated significant research on the dynamics of these discharges [6, 7]. The fluxes of ions and photons, and electric

[3] Author to whom any correspondence should be addressed.

fields in APPJs that arrive at the surface being treated typically have lower intensities than in dielectric barrier discharges (DBDs) [8]. However, with APPJs there may be more opportunity to controllably react plasma produced species with the ambient air to form reactive oxygen and nitrogen species (RONS) that are beneficial for surface treatment.

Typically, the plasma jet is a noble gas seeded with small amounts of O_2 or H_2O [9]. The noble gas flows through a capillary tube in which the discharge is formed and then flows into room air. In doing so, a rare-gas dominated channel in the air is hydrodynamically formed and through which the plasma produced reactive species flow. Mixing of the reactive species in the gas plume with the ambient air environment results in production of secondary species [10, 11]. Due to the gas flow and repetitive pulsing, the temperature in the effluent of the plasma jet is near ambient [12, 13].

The *plasma bullet* that propagates through the plasma plume is also known as a *guided ionization wave* or *guided streamer* [7]. The structure of the guided streamer is similar to a conventional atmospheric pressure streamer where space charge produced electric field enhancement in the head of the streamer generates an electron avalanche. The guided aspect of propagation results from the *E*/*N* (electric field/gas number density) required for avalanche being lower in the rare-gas dominated plume than in the surrounding air. The avalanche is then prevented from rapidly spreading laterally into the air.

As the plasma produced ions, electrons, and other excited species interact with the ambient air, other RONS are created. The RONS produced in this manner that are believed to be beneficial in biomedical applications include singlet delta molecular oxygen [$O_2(a^1\Delta_g)$] oxygen atoms (O), hydroxyl radicals (OH), ozone (O_3), hydrogen peroxide (H_2O_2) and nitric oxide (NO) [14]. Each species has specific roles in plasma treatment of tissue that can be leveraged independently or complement others, and whose production rates should ideally be separately controlled. For example, $O_2(a^1\Delta_g)$ is a metastable species that is a convenient mechanism to transport activation energy from the plasma to the surface. OH and O are oxidizing species. NO is an important cellular signaling molecule thought to be important in wound healing. Ozone is a convenient vehicle to transport the reactivity of the O atom to remote locations.

There are a variety of geometries and discharge production techniques for APPJs [9]. The effects of admixtures to the noble gas [15], use of shielding gases [16, 17], effects of positive and negative voltage pulses [18] and pulse repetition frequency [19] have been investigated in an effort to further understand and optimize the production of the RONS in APPJs [20]. Although the final desired outcome in the use of APPJs is typically to treat a surface, the first step in this process is to generate the reactive species in the gas phase through the repetitive sequence of electric discharge formation in the capillary, flow of primary reactive species into the rare-gas dominated plume, mixing with the ambient environment and transport to the surface.

In this paper, we report on a computational investigation of the production of reactive species in a repetitively pulsed APPJ sustained in He/O_2 mixtures. Many APPJs transition to turbulent flow due to the natural evolution of a jet flowing into stagnant air or through interaction with the plasma [21]. In this study, we have focused on purely laminar flows with the goal of providing further insights to the consequences of repetition rate, gas mixture, voltage, and flow rates. The simulations have also been performed for a jet into ambient air without intersecting a surface. Clearly the gas flow, mixing and subsequent reaction chemistry is affected by the perturbation of the flow by the surface. Our intent here is to investigate the process that delivers reactive species to the vicinity of the surface. In this regard, the flow distance modeled here is up to 8 cm with the rationale that the jet-to-surface distance is typically in the 1–10 cm range.

The model used in this investigation is described in section II. Results from our investigation are discussed in section III for a He/O_2 plasma jet flowing into room air produced a single and multiple discharge pulses (section IIIa), with different voltages (section IIIb), admixtures (section IIIc), flow rates (section IIId) and pulse repetition rates (section IIIe). Our concluding remarks are in section IV.

II. Description of the model

The 2D cylindrically symmetric model used in this investigation, *non-PDPSIM*, has been previously described [22, 23]. The model uses time-slicing techniques and an unstructured triangular mesh to bridge the sub-picosecond time steps necessary to resolve the discharge dynamics on micron spatial scales in the capillary tube during the discharge pulse, to the many microsecond timesteps over mm spatial scales up to many ms of elapsed time in the plume between and over many discharge pulses. In this investigation, a series of modules in *non-PDPSIM* are sequentially and iteratively executed.

In the plasma transport module, Poisson's equation and continuity equations for charged species are solved. The equation we solve is

$$\nabla\left(\varepsilon\ \nabla\Phi\right) = -\left(\sum_j q_j N_j + \rho_{\mathrm{M}}\right), \tag{1}$$

where ε is the permittivity, Φ is the electrical potential, q_j is the elementary charge, N_j is the species number density, and ρ_{M} is the charge on surfaces and in materials. Concurrent to solving Poisson's equation, we solve for the density of charged particles and charge densities in and on materials. For charged particle densities we solve

$$\frac{\partial N_j}{\partial t} = -\nabla\cdot\vec{\Gamma}_j + S_j + \left[\sum_m -\nabla\cdot\vec{\Gamma}_m\gamma_m + \sum_k -\nabla\cdot\phi_m\gamma_m\right]_b, \tag{2}$$

where the charged particle flux, Γ, is formulated using the method of Scharfetter and Gummel [24]. The source due to collisions is S_j. The sums in brackets apply only to electrons on the boundary of the plasmas for secondary electron emission by ions and excited species (first sum) and by photons with flux ϕ having secondary emission coefficient γ. The material charge density is solved using,

$$\frac{\partial \rho_M}{\partial t} = \left[\sum_j q_j \left(-\nabla \cdot \vec{\Gamma}_j (1+\gamma_j) \right) + \sum_k \phi_k \gamma_k \right] - \nabla \cdot (\sigma(-\nabla \Phi)), \quad (3)$$

where σ is conductivity of solid materials. The sums in brackets apply only to points on the surface of the material.

Equations (1)–(3) are implicitly solved using a Newton–Raphson iteration technique. Jacobian elements are generated for the incremental change in variable i at mesh point j due to a change in variable k at mesh point m, $\partial N_{ij}/\partial M_{km}$. The mesh points for which the Jacobian elements are produced are the local point and nearest neighbors. There are six nearest neighbors in the ideal triangle based mesh, however in practice the number of nearest neighbors varies from 4 to 10. The Jacobian element is produced by perturbing the value of the independent variable by a small amount. For example, the Jacobian element for the change in ion density N_{ij} at time t due to a perturbation of $\Delta\Phi$ in potential Φ_m during a time step of duration Δt is

$$\frac{\partial N_{ij}}{\partial \Phi_m}(t) = -\frac{\Delta t}{\Delta \Phi}(\nabla \cdot (\vec{\Gamma}_j(\Phi_m(t) + \Delta\Phi) - \vec{\Gamma}_j(\Phi_m(t)))). \quad (4)$$

The divergence operators are expressed in finite volume format,

$$\frac{\partial N_{ij}}{\partial t} = -\nabla \cdot \vec{\Gamma}_{ij} = \sum_m \frac{\Gamma_{ijm} A_{jm}}{V_j}, \quad (5)$$

where Γ_{ijm} is the flux from nearest neighbor cell m arriving into cell j, A_{jm} is the area of the face between numerical cells j and m, and V_j is the volume of cell j. The discretized partial differential equation then solved for species density is,

$$N_{ij}(t+\Delta t) = N_{ij}(t) + \Delta t \left(\sum_m \frac{\Gamma_{ijm}(N_j(t+\Delta t), \Phi(t)) A_{jm}}{V_j} + S_j(t) + \frac{\partial S_{ej}}{\partial n_e}(n_e(t+\Delta t) - n_e(t)) \right) + \sum_m \left(\frac{\partial N_{ij}}{\partial \Phi_m}(t)(\Phi_m(t+\Delta t) - \Phi_m(t)) + \frac{\partial N_{ij}}{\partial N_{im}}(t)(N_{im}(t+\Delta t) - N_{im}(t)) \right). \quad (6)$$

Source functions are evaluated at time t except for those involving electron impact processes which are evaluated at time $(t + \Delta t)$ through use of the Jacobian element $\partial S_{ej}/\partial n_e$. Similar expressions are generated for potential and charge density. The function that is minimized is during the kth Newton–Raphson iteration is

$$F_{ij} = \frac{[N_{ij}(t+\Delta t)]_k - [N_{ij}(t+\Delta t)]_{k-1}}{N_{0j}}, \quad (7)$$

where N_{0j} is a normalization value chosen so that all normalized variables have values close to unity. The values at $(t + \Delta t)$ are obtained by solving the combined sparse matrix using a two solver-preconditioner combination based on BiCG/ILUT. After each Newton–Raphson iteration, the Jacobian elements are re-evaluated with current values of variables.

Following the update of the electric potential and charged particle densities, the electron temperature is updated using

$$\frac{\partial}{\partial t}\left(\frac{3}{2} n_e k_B T_e\right) = S_P(T_e) - L_P(T_e) - \nabla \cdot \left(\frac{5}{2} \Gamma_e k_B T_e - \kappa(T_e) \cdot \nabla T_e \right), \quad (8)$$

where T_e is the electron temperature, n_e is the electron density, k_B is Boltzmann's constant, κ is the thermal conductivity, S_P is the sources of power, in this case, Joule heating from the electric field and L_P represents collisional losses or gains in energy. Equation (8) is implicitly solved using the method of successive-over-relaxation (SOR). The form solved is.

$$T_{ej}(t+\Delta t) = T_{ej}(t) + \frac{2\Delta t}{3 k_B n_{ej}(t+\Delta t)} \times \left[-\frac{\partial n_{ej}(t+\Delta t)}{\partial t} k_B T_{ej}(t+\Delta t) + \vec{\Gamma}_{ej} \cdot \vec{E}_j + \sum_i n_{ej}(t+\Delta t) N_{ij} \Delta \varepsilon_i \times \left(k_{ij}(T_{ej}(t)) + + \frac{\partial k_{ij}(T_{ej}(t))}{\partial T_e}(T_{ej}(t+\Delta t) - T_{ej}(t)) \right) + \sum_m \frac{A_{jm}}{V_j} \left(\frac{5}{2} \Gamma_{ejm}(t+\Delta t) T_{ejm}(t+\Delta t) + \kappa(t+\Delta t) \times (T_{em}(t+\Delta t) - T_{ej}(t+\Delta t)) \right) \right], \quad (9)$$

where $k_{ij}(T_e)$ is the rate coefficient for electron impact process i at mesh point j with change in energy $\Delta\varepsilon_i$ and the collision partner has density N_i. T_{ejm} indicates that the upwind value of the electron temperature is used—that is, the donor-cell method is employed. During the SOR iterations (typically hundreds of iterations are required per time step), the thermal conductivities and rate coefficients are updated every 10–20 iterations. Due to the computational expense of updating the rate coefficients on a more frequent basis, a correction to the rate coefficient for changes in T_e is accounted for by the Jacobian element $\partial k_{ij}(T_{ej}(t))/\partial T_e$. Convergence is determined by values of T_e only in those cells that have an electron density greater than a minimum value, typically 10^4–$10^5\,\mathrm{cm}^{-3}$.

The desired value of electric field used in equation (9) is at the mesh point j. Since the electric potential is solved at the mesh points, the electric fields are only directly available along the chords between mesh points. The electric fields components at j are obtained by interpolating the values of electric potentials from the nearest neighbor mesh points to the coordinate axes above and below, and to the left and right, of location j. Electric fields are then obtained by linear finite differencing of the interpolated values. A similar technique is used to obtain gradients in number densities at the mesh point j.

Rate and transport coefficients are obtained as a function of T_e by constructing a table through solving the stationary Boltzmann's equation over a range of E/N (electric field/gas

number density). The table typically consists of 70 entries over a range of E/N from 0.1 Td to 1000 Td (1 Td = 10^{-17} V cm^2). The entries in the table are recorded as log values and then linearly interpolated. The tables are updated during execution of the model as mole fractions of collision partners change. Different tables are constructed for different parts of the mesh that may have significantly different gas composition.

Individual neutral species diffuse within the single fluid flow field and react with surfaces. Their densities are updated using

$$\frac{\partial N_i}{\partial t} = -\nabla\cdot(N_i\overrightarrow{v}) - \nabla\cdot(-D_i\nabla N_i) + S_i + \left[\sum_k -g_{ki}\nabla\cdot\Gamma_k\right]_{ms}, \tag{10}$$

where, $\overrightarrow{v}$ is the advective fluid averaged velocity, described below, D_i is the mixture dependent diffusivity, and S_i is the source or sink of that neutral species by collisions. The term in brackets accounts for the flux of species k reacting on material surfaces to produce species i with probability g_{ki}. Equation (10) is also solved implicitly using the method of successive over relaxation,

$$N_{ij}(t+\Delta t) = N_{ij}(t) + \Delta t\left[\sum_m \frac{A_{jm}}{V_j}(D_{ijm}(N_{im}(t+\Delta t) - N_{ij}(t+\Delta t)) + v_{jm}N_{ijm}(t+\Delta t)) + S_i(t) + \left[\sum_{m,k} -\frac{A_{jm}}{V_j}g_{ki}\Gamma_k(t+\Delta t)\right]_m\right]. \tag{11}$$

Radiation transport and photoionization are addressed using a Green's function approach. The photoionization source for species i at location $\vec{r}_j$ is due to the integral of vacuum ultraviolet (VUV) photon emission at all other locations $\vec{r}_l$ is

$$S_{Pi}(\vec{r}_j) = N_i(\vec{r}_j)\cdot\sum_k \sigma_{ik}A_k\int N_k(\vec{r}_l^{\,'})G_{ilk}(\vec{r}_l^{\,'},\vec{r}_j)\,\mathrm{d}^3\vec{r}_l^{\,'}, \tag{12}$$

where σ_{ik} is the photoionization cross section of the species i by the photon generated by species k, A_k is the Einstein A coefficient for the transition. G_{kil} is the Greens function that provides the relative flux of the photon emitted at $\vec{r}_l$ that survives to reach $\vec{r}_j$.

$$G_{kil}(\vec{r}_i,\vec{r}_l) = \frac{\exp\left(-\int_{\vec{r}_l}^{\vec{r}_i}\sum_n \sigma_{kn}N_n(\vec{r}_p^{\,'})\mathrm{d}\vec{r}_p^{\,'}\right)}{4\pi\left|\vec{r}_i^{\,'}-\vec{r}_l\right|^2}, \tag{13}$$

where the integral in the exponent accounts for absorption by any process of photon k by species N_n with cross section σ_{kn}. The photoionization processes included in the model are the photon producing decay of the excited Helium dimer $He_2^* \rightarrow He + He + h\nu$ and the subsequent ionization of the oxygen molecule $O_2 + h\nu \rightarrow O_2^+ + e$.

Generating G_{kil} in the unstructured mesh in large part consists of evaluating the integral within the exponent. The integral is evaluated in the following manner. A chord is drawn between the emitting node l from which the photon originates and the absorbing node j where the photoionization occurs. The emitting node l is the *base* node. The two nodes of the nearest neighbors to l on either side of the chord are determined and the intersection of the line between the neighbors and the chord is determined. If the intersection is inside an absorbing material, then the photon is blocked and $G_{kil} = 0$. If the intersection is inside the plasma the density of density of N_n is interpolated to the intersection and the integral incremented based on the distance from the base node. The nearest neighbor of the base node l to the intersection is then the new base node, and the process is repeated until node j is reached. Generating the Green's function is computationally expensive and so G_{kil} is not recomputed unless the density of absorbers significantly changes.

Using unsteady, compressible algorithms, *non-PDPSIM* updates the neutral fluid mass, momentum and energy equations using time slicing between the plasma modules using a fully implicit, sparse matrix technique [22]. Due to the significant differences in mass density resulting from the He jet emanating into air, the traditional Navier–Stokes like equations are modified in the following manner. The continuity equations are

$$\frac{\partial N_t}{\partial t} = -\nabla\cdot\left(N_t\vec{v} + \sum_{k,i}\frac{f_{ki}}{A_k}\right), \tag{14}$$

$$\frac{\partial N_tM_t}{\partial t} = -\nabla\cdot\left(\sum_i m_i\Gamma_iN_i + \sum_{k,i}\frac{m_if_{ki}}{A_k}\right), \tag{15}$$

where N_t is the total number density of atoms and molecules in the gas, $\overrightarrow{v}$ is the advective velocity and the sum in equation (14) is over gas inlets k having face area A_k where species i has an inlet flow rate f_{ki}. Equation (15), provides the average molecular weight M_t where m_i is the molecular weight of species i having flux Γ_i and density N_i.

The momentum equation is then

$$\frac{\partial(N_tM_t\vec{v})}{\partial t} = -\nabla P - \nabla\cdot(M_tN_t\vec{v}\vec{v}) - \nabla\cdot\overline{\tau} + \sum_i q_iN_i\vec{E} + N_tM_tg\frac{\overrightarrow{v}\cdot\hat{n}}{|\overrightarrow{v}|} \tag{16}$$

where $\overline{\tau}$ is the stress tensor, q_i is the elementary charge, g is the gravitational constant, $\hat{n}$ is the normal in the direction of gravity, $\vec{E}$ is the electric field and N_i is the number density of species i. We assumed ideal gas properties so the pressure $P = N_tk_BT$. The term with the electric field represents the net momentum transfer between charged particles accelerated by the electric field and the neutral gas.

In the conservation of energy equation,

$$\frac{\partial(N_tc_vT)}{\partial t} = -\nabla(-\kappa\nabla T + \rho\vec{v}c_vT) + P\nabla\cdot\vec{v} - \sum_m R_m\Delta H_m + \sum_i\vec{j}_i\cdot\vec{E}, \tag{17}$$

c_v is the specific heat, κ is the thermal conductivity, T is the gas temperature, R_m is the rate of reaction m, ΔH_m is the change in enthalpy for reaction m (including electron elastic and dissociative excitation collisions), and $\vec{j}_i \cdot \vec{E}$ is the Joule heating term where the sum is over ions having current density $\vec{j}_i$. Assuming no slip conditions at atmospheric pressure, the boundary conditions are that the temperature matches the wall temperature. Although not used here, there is also the option to retain the thermal conduction term of equation (17) inside materials and compute temperature throughout materials. In this case, additional heating terms are added at surfaces for the change in enthalpy due to the recombination of ions and other surface chemistry. In this case the temperature is held constant at the periphery of the mesh.

Equations (14)–(17) were implicitly solved using sparse matrix techniques in a similar manner as for the charged particle transport equations. For brevity, we will only describe the solution method for the axial component of momentum in equation (16). With $\rho_t = N_t M_t$ $p_z = N_t M_t v_z$, $\Delta M = M(t+\Delta t) - M(t)$, M any quantity, and $\varepsilon = N_t c_v T$, we solve for component p_z at mesh point j having neighbor nodes m

$$
\begin{aligned}
p_{zj}(t+\Delta t) = p_{zj}(t) + [& -\frac{\partial}{\partial z}\left(P(t)\Delta t \cdot + \left(\frac{\partial P}{\partial \rho_t}(t)\right)\Delta\rho_t + \left(\frac{\partial P}{\partial T}(t)\right)\Delta T \right) \\
& + \sum_m \frac{A_{jm}}{V_j} \begin{pmatrix} -p_{zj}(t+\Delta t)\delta_{jm}\left(\left(\vec{v}_j(t)\Delta t + \left(\frac{\partial \vec{v}_j}{\partial \rho_t}(t)\right)\Delta\rho_{tj} + \left(\frac{\partial \vec{v}_j}{\partial T}(t)\right)\Delta T_j\right)\cdot \widehat{n}_{jm}\right) \\ +p_{zm}(t+\Delta t)\delta_{mj}\left(\left(\vec{v}_m(t)\Delta t + \left(\frac{\partial \vec{v}_m}{\partial \rho_t}(t)\right)\Delta\rho_{tm} + \left(\frac{\partial \vec{v}_m}{\partial T}(t)\right)\Delta T_m\right)\cdot \widehat{n}_{mj}\right) \end{pmatrix} \\
& - \left(\nabla \cdot \left(\overline{\tau}\Delta t + \left(\frac{\partial \overline{\tau}}{\partial \rho_t}(t)\right)\Delta\rho_t + \left(\frac{\partial \overline{\tau}}{\partial T}(t)\right)\Delta T \right) \cdot \right)_z + \sum_i q_i N_i(\vec{E}(t)\cdot\widehat{z}) + N_t M_t g(\widehat{z}\cdot\hat{n}),
\end{aligned}
\tag{18}
$$

where $\widehat{n}_{jm}$ is the unit vector pointing along the chord from j to m. In the divergence operator having the sum over nearest neighbors, the donor-cell method is used. The coefficient δ_{jm} is unity if $\vec{v}_m \cdot \widehat{n}_{jm}$ is positive and zero otherwise. As in the transport equations for charge, spatial gradients are produced by interpolating nearest neighbor values to the coordinate axis above and below (and to the right and left of) the mesh point, and then differentiating the interpolated values.

Due to the unstructured nature of the mesh, densities, velocities (momenta) and temperatures are all directly computed at the mesh points. (In structured meshes, it is more common to compute momenta along the chord between mesh points.) The inlet boundary conditions on flow consist of specifying the fluxes perpendicular to the face of the gas nozzles and their average molecular weight is based on the mole fractions and molecular weights of the inlet gases. The outlet boundary condition is a specified pressure on the face of the pump ports and this pressure is directly incorporated into equation (16). A check is made on the normal velocity into the pump port and this velocity is required to be positive.

The process of simulating the discharge pulse and afterglow is as follows. The simulation begins by first computing the advective flow field solving only equations (14)–(17) using time steps of about 1 μs. These small time steps are required by the small dimensions of the mesh inside the tube. After the flow field is established, voltage is applied to the electrode and all modules of the model are then executed. The time steps for the plasma module, including solution of the electron energy equation and photon-transport are 0.1–5 ps. The table of electron transport coefficients is updated by re-solving Boltzmann's equation every 0.05 ns. The fluid module is executed every 0.05 ns. This process is continued for 80 ns (see below). At that point, the voltage pulse is terminated and Poisson's equation is no longer solved. A quasi-neutral assumption is then made which enables the time steps to greatly increase. From the time that Poisson's equation is no longer solved to tens to hundreds of μs later, the timestep increases from <1 ns to $\approx 1\,\mu$s, a value constrained by the small size of the mesh inside the tube and the reaction rates of short lived species.

Multiple discharge pulses are addressed in the following manner. Recomputing the discharge for every pulse is computationally intensive and would be prohibitive for the many tens of pulses and parametric study considered here. The length of time that species are produced by electron impact processes during the discharge pulse is tens of ns whereas the interpulse periods are hundreds of μs to ms, and gas residence times are many ms to tens of ms. On the timescale of the flow, the electron impact generated sources appear nearly instantaneously. During the first discharge pulse which is fully resolved in the manner described above, the source functions by electron impact, photoionization and fast neutral reactions are integrated in time. On the second and subsequent pulses we add in these sources functions to the continuity equations as an impulsive source of species. The strength of this method is that many tens to hundreds of pulses can be addressed. The weakness of the method is that modifications to the source functions due to the changing composition of the gas on a pulse-by-pulse basis are not addressed. For high flow rates and low repetition rates which produce short residence times of gas in the discharge tube relative to the interpulse period, this is not a particularly large effect. For these conditions, the gas is nearly refreshed inside the tube between pulses. For low flow rates and high repetition rates which produce long residence times relative to the interpulse period, the gas is not refreshed inside the tube and so some accuracy is lost.

The reaction mechanism includes over 50 species and more than 750 reactions. A discussion of the full reaction mechanism of electron impact processes, ion–ion neutralization, ion–molecule reactions, Penning ionization, quenching, three-body neutral recombination, and neutral chemistry has been the topic of several recent investigations [25–30] and we will not repeat that discussion here. We would, however, like to emphasize the reaction mechanism leading to a selected subset of RONS that will be discussed in this paper. The primary paths to these RONS are highlighted in table 1.

The first path is to ozone, O_3 and starts with the production of O atoms from electron dissociative excitation and dissociative attachment of O_2 (R1)–(R3) within the active plasma plume. There are also small contributions to production of O atoms from dissociative recombination of O_2^+. Three body collisions of O and O_2 then produce O_3 (R8). This process is slow in the active plasma inside the discharge tube due to the low mole fraction of O_2. Other direct sources of O_3 in the active plasma include electron detachment reactions of O_2^- and O^- (R6)–(R7). In the effluent, the primary source of O atoms is the dissociative quenching of N_2^* by O_2 (R5) that forms two O atoms. The previously formed O atoms from inside the tube that are carried with the flow and newly formed O atoms outside the tube react with the increasing mole fraction of O_2 due to diffusion and mixing with the ambient air. In the absence of organic molecules, O_3 is a fairly stable species. It is primarily consumed by reactions with excited nitrogen, NO, and NO_2 (R24), (R27), (R29), (R33), (R39) to form NO and higher N_xO_y.

Another important RONS formed by the plasma jet is hydrogen peroxide, H_2O_2. In the absence of hydrogen containing species in the gas feed, the path to H_2O_2 originates with the humidity in the air. The water vapor diffusing into the active plasma plume undergoes dissociative excitation and attachment to produce the hydroxyl radical, OH (R9), (R10). Another source of OH is the ion–ion neutralization of O_2^- and H_2O^+ (R12) which occurs in the near effluent shortly after the ionization wave propagates. The third-body assisted reaction of two OH radicals then forms H_2O_2 (R13). Again, in the absence of organic molecules, H_2O_2 is fairly stable. Most destruction mechanisms of H_2O_2 require higher temperatures than encountered in plasma jets.

The path to nitric oxide, NO, starts with electronic excitation of N_2 to form N_2^* (the sum of $N_2(A^3\Sigma)$ and $N_2(B^3\Pi)$ in this mechanism) and N_2^{**} (the sum of $N_2(C^3\Pi)$ and higher states) (R14), (R15). These excited states then react with O atoms and O_3 to form NO (R25)–(R29). Additional routes to NO first include the dissociative excitation of N_2 (R16) or the rapid ion–ion neutralization of O_2^- and N_2^+ (R17) to form N atoms. Subsequent reactions with O, O_2, $O_2(^1\Delta)$, $O_2(^1\Sigma)$, O_3 and OH form NO (R18)–(R23). Nitric oxide is the primary source for higher level oxides of nitrogen (N_xO_y) (R30)–(R44). The nitric oxide acids, HNO_x, form primarily from the reaction of NO or N_xO_y with OH in three-body collisions (R49, R51, R53).

III. Dynamics of plasma jet

The experimental configuration we modeled is a cylindrically symmetric tube with an inner pin electrode as shown in figure 1. Helium seeded with oxygen flows vertically through the tube into humid air. The inner diameter of the tube of 1.6 mm and length of 7 mm are roughly based on the dimensions of the kINPen plasma source [16, 17] The axial location of the powered electrode was based on various experiments of atmospheric pressure plasma jets [13, 40]. The pin electrode has a radius of 0.25 mm. The entire computational domain shown in figure 1(a) is 2 cm by 10 cm and contains over 22 000 numerical mesh nodes with 20 000 being in the plasma or gas. (The plasma jet is shown in the lower right corner of figure 1(a).) The ring around the dielectric tube is treated as a dielectric as well. The minimum cell size inside the tube near the electrodes is 36 μm. The maximum cell size in the periphery of the mesh is 400 μm. The outer radial wall is dielectric and the top surface is grounded metal which also serves as the pump. The mesh is finest near the pin electrode and has a series of refinement zones that gradually increase the spacing of the mesh in the path of the ionization wave, shown in figure 1(b). The He/O_2 mixture is injected through the annular face between the pin electrode and the tube. Humid air is flowed into the volume through the annular face on the bottom boundary outside of the tube and inside of the outer wall. This slowly flowing shroud of ambient gas helps stabilize the jet and minimize the formation of vortices. The inlet and shroud gases are initially flowed for 50–80 ms to establish a steady state flow field prior to the discharge being ignited.

The base case has He/O_2 = 99.8/0.2 at atmospheric pressure flowing through the tube at 4 slm into the humid room air ($N_2/O_2/H_2O$ = 79.5/20/0.5). The flow of the humid air shroud is 4 slm. A single −15 kV pulse 80 ns long is applied (5 ns rise and 75 ns duration at the specified voltage with immediate drop to zero). Subsequent parameterizations from the base case will vary flow rate (2–7 slm), the admixture of O_2 (0.1–2%), applied voltage (−10 to −30 kV), and pulse repetition frequency—PRF (5–500 kHz).

IIIa. Base case

The concentrations of He, N_2, O_2 and H_2O as the injected gases flow into the ambient are shown in figure 2 for the base case at the time that the discharge is initiated. (The O_2 concentration is shown over three orders of magnitude to capture the seed oxygen in the helium.) With flow distance from the end of the tube, air diffuses into the He plume as He diffuses into the ambient. The 4 slm flow rate for the base case and a tube radius of 1.6 mm produces a speed of the helium mixture through the tube of 42 m s^{-1}. This speed corresponds to a Reynolds number for the helium gas of 630 indicating laminar flow. For pipe flow, the transition to turbulent flow occurs at 2300. Once the jet leaves the tube the onset of turbulence will begin at about $50r_0$ from the outlet,

Table 1. Critical reaction pathways to form the near-terminal RONS O_3, N_xO_y, H_2O_2 and HNO_x.

	Reaction[a]	Reaction rate[b]	Ref.
	***Path to* O_3**		
(R1)	$e + O_2 \rightarrow O + O + e$		[31][c]
(R2)	$e + O_2 \rightarrow O^* + O + e$		[31][c]
(R3)	$e + O_2 \rightarrow O^- + O$		[31][c]
(R4)	$O_2^- + O_2^+ \rightarrow O_2 + O + O$	1×10^{-7}	[28]
(R5)	$N_2^* + O_2 \rightarrow O + O + N_2$	1.5×10^{-12}	[32]
(R6)	$O_2^- + O \rightarrow O_3 + e$	1.5×10^{-10}	[28]
(R7)	$O^- + O_2^* \rightarrow O_3 + e$	3×10^{-10}	[28]
(R8)	$O + O_2 + M \rightarrow O_3 + M$	$3.4 \times 10^{-34}\,(T_g/300)^{-1.2}$	[33]
	***Path to* H_2O_2**		
(R9)	$e + H_2O \rightarrow H + OH + e$		[34][c]
(R10)	$e + H_2O \rightarrow H^+ + OH + e + e$		[34][c]
(R11)	$e + H_2O^+ \rightarrow OH + H$	$6.6 \times 10^{-6} T_e^{-0.5}$	[35]
(R12)	$O_2^- + H_2O^+ \rightarrow O_2 + OH + H$	1×10^{-7}	[28]
(R13)	$OH + OH + M \rightarrow H_2O_2 + M$	$6.9 \times 10^{-31}\,(T_g/300)^{-0.8}$	[33]
	***Path to* N_xO_y[a]**		
(R14)	$e + N_2 \rightarrow N_2^* + e$		[36][c]
(R15)	$e + N_2 \rightarrow N_2^{**} + e$		[36][c]
(R16)	$e + N_2 \rightarrow N + N + e$		[36][c]
(R17)	$O_2^- + N_2^+ \rightarrow O_2 + N + N$	1×10^{-7}	[28]
(R18)	$N + O + M \rightarrow NO + M$	$5.46 \times 10^{-33} \exp(155/T_g)$	[33]
(R19)	$N + O_2 \rightarrow NO + O$	$4.4 \times 10^{-12}\,(T_g/300)\exp(-3270/T_g)$	[33]
(R20)	$N + O_3 \rightarrow NO + O_2$	5×10^{-16}	[33]
(R21)	$N + OH \rightarrow NO + H$	4.7×10^{-11}	[33]
(R22)	$N + O_2^* \rightarrow NO + O$	$2 \times 10^{-14} \exp(-600/T_g)$	[29]
(R23)	$N + O_2\,(^1S) \rightarrow NO + O$	2.5×10^{-10}	[37]
(R24)	$N^* + O_3 \rightarrow NO + O_2$	1×10^{-10}	[29]
(R25)	$N_2^* + O \rightarrow NO + N$	5×10^{-10}	[38]
(R26)	$N_2^* + O \rightarrow NO + N^*$	1×10^{-12}	[29]
(R27)	$N_2^* + O_3 \rightarrow NO + NO + O$	8.4×10^{-12}	[29]
(R28)	$N_2^{**} + O \rightarrow NO + N$	5×10^{-10}	[38]
(R29)	$N_2^{**} + O_3 \rightarrow NO + NO + O$	8.4×10^{-12}	[29]
(R30)	$O_2^- + N \rightarrow NO_2 + e$	5×10^{-10}	[28]
(R31)	$NO + O + M \rightarrow NO_2 + M$	$1 \times 10^{-31}\,(T_g/300)^{-1.6}$	[33]
(R32)	$NO + O_2^* \rightarrow O + NO_2$	4.88×10^{-18}	[33]
(R33)	$NO + O_3 \rightarrow O_2 + NO_2$	$1.4 \times 10^{-12} \exp(-1310/T_g)$	[33]
(R34)	$NO + HO_2 \rightarrow NO_2 + OH$	8.8×10^{-12}	[33]
(R35)	$NO + NO + O_2 \rightarrow NO_2 + NO_2$	2×10^{-38}	[33]
(R36)	$NO_2 + O \rightarrow NO + O_2$	$6.5 \times 10^{-12} \exp(120/T_g)$	[29]
(R37)	$NO_2 + H \rightarrow NO + OH$	1.28×10^{-10}	[33]
(R38)	$NO_2 + O + M \rightarrow NO_3 + M$	$9 \times 10^{-32}\,(T_g/300)^{-2}$	[33]
(R39)	$NO_2 + O_3 \rightarrow O_2 + NO_3$	$1.4 \times 10^{-13} \exp(-2470/T_g)$	[29]
(R40)	$NO + NO_3 \rightarrow NO_2 + NO_2$	$1.6 \times 10^{-11} \exp(150/T_g)$	[33]
(R41)	$NO_3 + NO_3 \rightarrow NO_2 + NO_2 + O_2$	1.2×10^{-15}	[39]
(R42)	$NO + NO_2 + M \rightarrow N_2O_3 + M$	3.1×10^{-34}	[33]
(R43)	$NO_2 + NO_2 + M \rightarrow N_2O_4 + M$	1.4×10^{-33}	[33]
(R44)	$NO_2 + NO_3 + M \rightarrow N_2O_5 + M$	3.6×10^{-30}	[33]
	***Path to* HNO_x[a]**		
(R45)	$N_2O_3 + H_2O \rightarrow HNO_2 + HNO_2$	1.93×10^{-17}	[33]
(R46)	$N_2O_4 + H_2O \rightarrow HNO_2 + HNO_3$	1.33×10^{-18}	[33]
(R47)	$N_2O_5 + H_2O \rightarrow HNO_3 + HNO_3$	2×10^{-21}	[33]
(R48)	$NO + NO_2 + H_2O \rightarrow HNO_2 + HNO_2$	5.55×10^{-34}	[33]
(R49)	$NO + OH + M \rightarrow HNO_2 + M$	6×10^{-31}	[33]
(R50)	$NO + HO_2 + M \rightarrow HNO_3 + M$	2×10^{-30}	[33]
(R51)	$NO_2 + OH + M \rightarrow HNO_3 + M$	1.7×10^{-30}	[33]
(R52)	$HO_2 + NO_2 \rightarrow HNO_2 + O_2$	1.2×10^{-13}	[33]
(R53)	$NO_2 + OH + M \rightarrow ONOOH + M$	3.37×10^{-30}	[33]
(R54)	$NO + HO_2 \rightarrow ONOOH$	6.09×10^{-11}	[33]

[a] O* represents O(^{1}D), O_2^* represents $O_2(a^1\Delta_g)$; N_2^* represents $N_2(A^3\Sigma, B^3\Pi)$; N_2^{**} represents $N_2(C^3\Pi$, and higher); M represents total gas density; N_xO_y represents NO_2, NO_3, N_2O_3, N_2O_4 and N_2O_5; HNO_x represents HNO_2, HNO_3 and ONOOH.

[b] Units are $cm^3\,s^{-1}$ for two-body reactions and $cm^6\,s^{-1}$ for three-body reactions.

[c] Rate coefficient obtained from solution of Boltzmann's equation for the electron energy distribution. Cross section was obtained from cited reference.

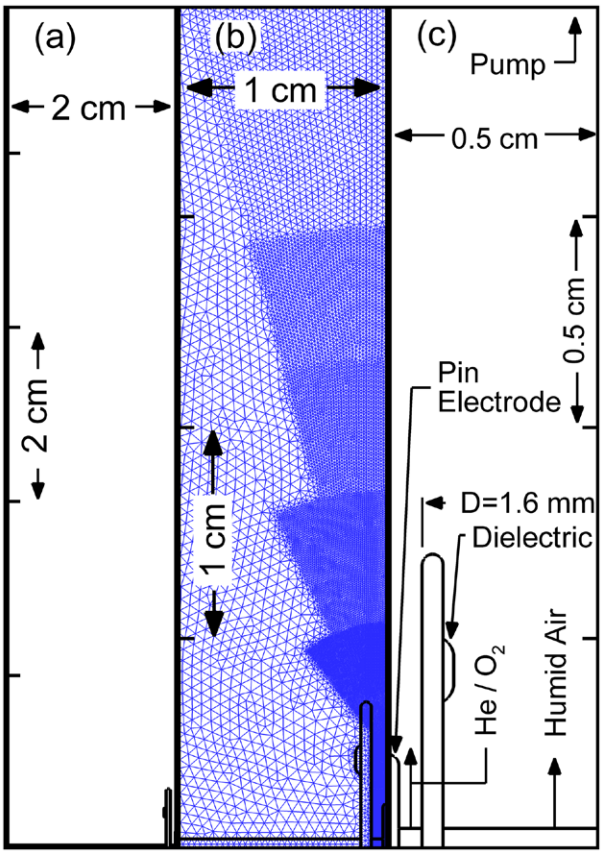

Figure 1. Schematic of the cylindrically symmetric plasma jet. (a) The full computational domain is 10 cm by 2 cm. (b) The numerical mesh with refinement zones. (c) Enlargement of the discharge tube.

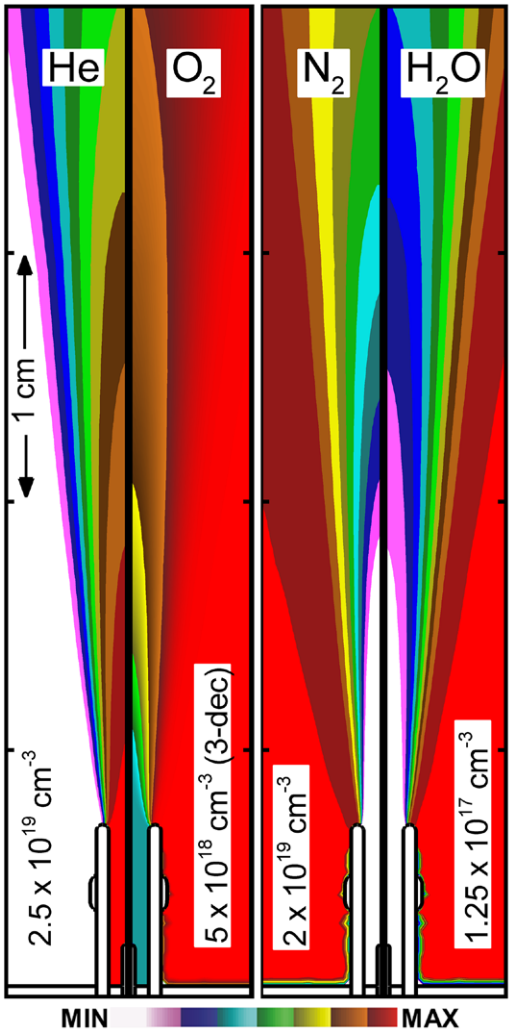

Figure 2. He, O_2, N_2 and H_2O concentrations for a flow rate of 4 slm (base case) through the tube and 4 slm in the shroud prior to discharge ignition. The O_2 concentration is over 3 decades from the maximum of 5×10^{18} cm^{-3} to highlight the seeded O_2 flowing with the He.

where r_0 is the jet radius [41]. This corresponds to about 4 cm for our conditions. The flow distances beyond the tube do not exceed 4 cm for the majority of our cases and not beyond 5–6 cm for a few select cases. For these select cases, we may be approaching turbulent conditions. For all cases, humid air flows outside the tube as a shroud at 4 slm with a corresponding speed of less than 1 m s^{-1}. The room air is entrained into the jet of helium, thereby enabling reaction with the plasma excited species.

The electron temperature, T_e, electron impact ionization source, S_e, and electric potential contours for the base case,−15 kV, are shown in figure 3(a) for 20 (T_e only), 50 and 80 ns. Note that these figures show a small sub-region of the entire computational domain. Early during the discharge pulse at 20 ns, the plasma is still largely contained within the tube. At this time, a cathode fall of 3 kV has already been established. As time increases, the guided ionization wave (represented by T_e and S_e) propagates out of the tube and into the previously established helium channel. The shape of T_e as well as the elongated ionization source for this negative streamer resembles those observed in experiments [18, 42] and as predicted by Naidis for a negative streamer [43]. T_e is 5 eV near the front of the propagating ionization wave. At the termination of the pulse, T_e decreases to 3.3 eV, and into a range that agrees with those measured by experiments [6, 15]. The velocity of the ionization wave is 1×10^7 cm s^{-1} which also agrees well with observed values [5, 18]. The speed of the ionization front should not be considered a universal value but rather is a sensitive function of the proximity of ground planes [44]. In the conductive plasma channel behind the ionization wave, the normalized electric field drops to $E/N = 10^{-17}$ V cm^{-2} (1 Td), resulting in T_e falling to <0.5 eV. Without the close proximity of an electrically grounded surface, the intensity of the plasma in the effluent remains weak and the length of the plume shorter. The predicted shape and length of the guided streamer are similar to those observed for APPJs propagating into the atmosphere far from an electrical ground plane [16]. When the same device is moved near a grounded surface, the emission intensity of the guided streamer increases and a conduction channel appears to form [45, 46].

The electron density, n_e, during the discharge pulse and the total positive ion density at 80 ns are shown in figure 3(b). Ion and selected excited state and radical densities are shown in figure 4(a). At 50 ns, the electrons have separated from the cathode forming a cathode fall-like sheath of nearly 200 μm around the electrode. The highest electron density is at the

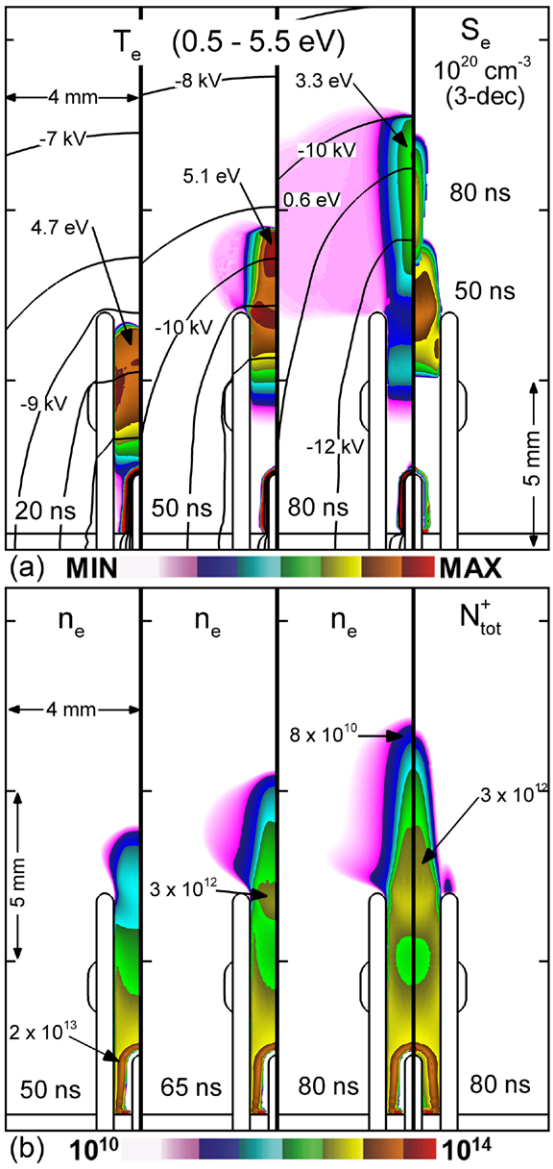

Figure 3. Plasma dynamics for the base case of $He/O_2 = 99.8/0.2$ at 4 slm with −15 kV applied for 80 ns. (a) Electron temperature T_e from left to right at 20, 50 and 80 ns on a linear scale between 0.5–5.5 eV. Potential contours are at 1 kV intervals. The electron impact ionization source S_e, is shown in the right frame at 50 and 80 ns using a log scale. (b) Electron density showing the propagation of the ionization wave into the effluent at 50, 65 and 80 ns. The cation density at 80 ns is the right image. Contours are on a four decade log-scale.

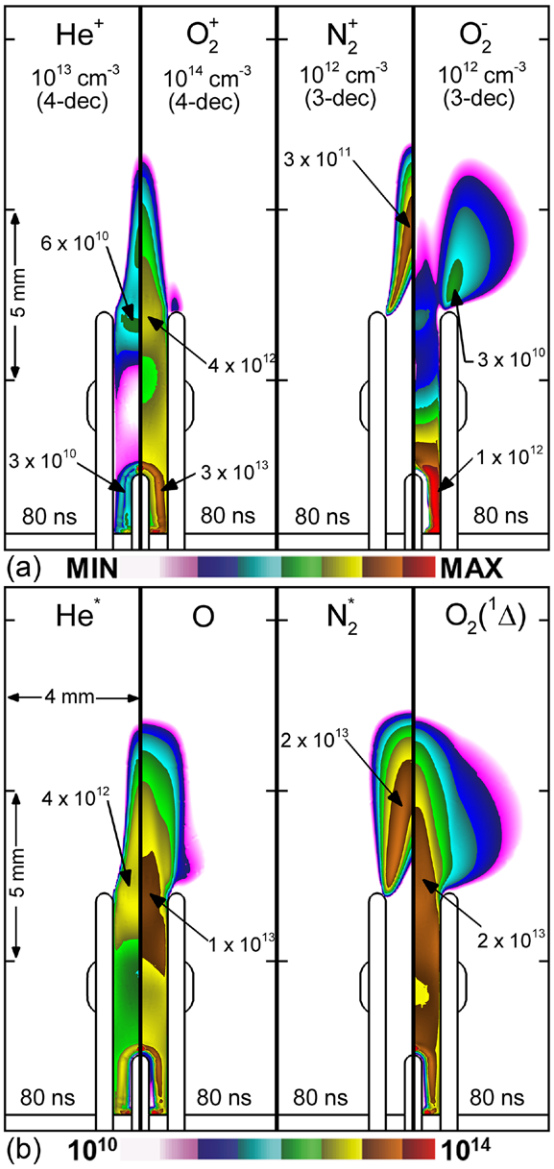

Figure 4. Reactant densities for the base case at 80 ns for the first discharge pulse. (a) Cation and anion densities. (b) Densities of primary excited states and reactive species. Excited helium density, He*, is the sum of $He(2^1S)$, $He(2^1P)$, $He(2^3S)$, $He(2^3P)$, He(3S) and He(3P) states. The excited molecular nitrogen, N_2^*, represents $N_2(A^3\Sigma, B^3\Pi, C^3\Pi$, and higher) and follows from the ionization wave intersecting the N_2 from the ambient diffusing into the plume. The lateral spread of $O_2(^1\Delta)$, indicates the laterally spreading of low energy electrons. Contours are on a four decade log-scale.

edge of the cathode fall, up to $10^{14}\,cm^{-3}$. The peak concentration in the tube outside the sheath and is $(2–5) \times 10^{13}\,cm^{-3}$. Within the effluent, the maximum is $3 \times 10^{12}\,cm^{-3}$. The majority of the electrons that have avalanched away from the cathode initially move toward and propagate along the wall of the tube, forming the annular appearing discharge observed and predicted by others [42, 43]. At 80 ns, the ionization wave has propagated out of the tube and the electron density has transitioned onto the axis. This transition is in part due to the diffusion of air into the jet that reduces the mole fraction of helium at larger radii. The infusion of air increases electron losses due to attachment and electron energy losses due to excitation of low lying vibrational and electronic states in the molecular gases, both of which increases the T_e (or E/N) required to sustain the plasma above those values that are available. The end result is that the ionization wave is restricted to being on axis. The on-axis electron density a few mm outside the tube is $10^{12}\,cm^{-3}$.

The electrons do spread laterally at the exit of the tube leading to a halo of negative ions with peak value of $3 \times 10^{10}\,cm^{-3}$. These negative ions are in large part generated by diffusion of electrons at the periphery of the streamer and photoionization which produce electrons in a region of low E/N (and low T_e) which then quickly attach. This halo of

low energy electrons having $T_e < 0.8$ eV are able to produce $O_2(^1\Delta)$ having a threshold energy of 1 eV but are less able to produce $N_2(A)$, having a threshold energy of 6 eV.

Ions produced by the ionization wave are shown at 80 ns in figure 4(a). The dominant cation is O_2^+ with a density of 3×10^{13} cm^{-3} at the edge of the sheath and 4×10^{12} cm^{-3} in the effluent. In spite of the mole fraction of O_2 in the tube being only 0.2%, the power flow favors formation of O_2^+. For example, for T_e =5 eV (E/N = 25 Td) and an He/O_2 = 99.8/0.2 gas mixture, the fraction of power dissipation directly producing O_2^+ by electron impact is 1.5%. The fraction of power directly populating excited states of He is 72% and directly producing He^+ is 3.6%. (These values were obtained from stationary solutions of Boltzmann's equation for the electron energy distribution.) The lifetime for Penning ionization for the He excited states and charge exchange from He^+ and He_2^+ is 40–70 ns to form O_2^+, commensurate with the length of the discharge pulse [26, 29]. So the majority of power dissipated into He is transferred to O_2 during the discharge pulse.

The N_2^+ density is maximum at 3×10^{11} cm^{-3}, extending from the edge of the tube to near the axis. This distribution of N_2^+ reflects the intersection of the N_2 diffusing into the plume from the humid air, the ionization wave propagating at this point along the axis and the He excited states and ions that form N_2^+ through Penning ionization and charge exchange, respectively. The lifetime for formation of N_2^+ by these processes at the location of the peak N_2^+ density is hundreds of ns. N_4^+ (not shown) follows the same trends as N_2^+ with a peak density of 3×10^{11} cm^{-3} at the end of the discharge pulse. The lifetime for formation of N_4^+ at the location of peak N_2^+ density is 100 ns. The density of He^+ in figure 4(a) decreases during the discharge pulse from 2×10^{11} cm^{-3} at 70 ns to 6×10^{10} cm^{-3} at 80 ns through recombination, formation of He_2^+ and charge exchange. The density of He_2^+ (not shown) remains relatively stable at 1×10^{11} cm^{-3}.

The neutral species that are the precursors to formation of RONS in the plume at the end of the discharge pulse (80 ns) are shown in figure 4(b). The He* is the sum of all He excited states (He(2^1S), He(2^1P), He(2^3S), He(2^3P), He(3S), He(3P)) and has a density of 4×10^{12} cm^{-3} in the effluent. These states are dominantly formed through electron impact of the ground state though there is a minor contribution from recombination of He^+ and He_2^+, no more than 1% of the total. Penning ionization from He* dominantly forms O_2^+, N_2^+ and H_2O^+. The density of He_2^* (not shown) at this time at the same location as shown for He* in figure 4(b) is 3×10^{10} cm^{-3}.

The RONS formed by this single pulse up to 80 ns can be placed into two categories—formation in the capillary tube dominantly by electron impact and formation by interaction of plasma activated species with the air diffusing into the plume. When the discharge is initiated, the O_2 in the feed gas undergoes electron impact dissociative excitation and attachment to form O in the tube. The highest density of O formed by this process, 1×10^{14} cm^{-3}, occurs near the tip of the pin electrode. The formation of O atoms by electron impact in the tube generally follows the electron density up the length of the tube and into the ambient producing an O atom density of 1×10^{13} cm^{-3} at the exit of the tube. Due to the low density of O_2 and lack of other species (such as H_2O) in the tube, the depletion of O by reactions in the tube is small. For example, the lifetime of O atoms for formation of O_3 in the tube is 1–2 ms. Meanwhile, other sources of O atoms, such as electron–ion recombination ($e + O_2^+ \rightarrow O + O$), continue to contribute to its density. This situation continues until diffusion of the humid air into the plume enables other reactions. As a result, the O atoms continue to accumulate from 80 ns to 1 μs. This accumulation of O atoms is aided by the quenching of N_2^* (which represents the sum of $N_2(A^3\Sigma$, $B^3\Pi$, $C^3\Pi$) and higher states)) by O_2 which produces O atoms [32]. The rate coefficient for dissociative quenching of N_2^* by O_2 is 1.5×10^{-12} cm^3 s^{-1} which accounts for the majority of production of O atoms where the ionization wave has produced significant densities of N_2^* [32].

The distribution of $O_2(^1\Delta)$ also follows the path of the electrons as $O_2(^1\Delta)$ is formed initially from electron impact excitation of ground state O_2. Its density grows to a maximum of 2×10^{13} cm^{-3} in the effluent near the exit of the tube at the end of the discharge pulse. An additional source of $O_2(^1\Delta)$ is the three-body recombination of O atoms, but this is a minor source due to the low density of O atoms. The radial spread of $O_2(^1\Delta)$ in the effluent above the tube results from the low energy electrons in the halo and the increasing O_2 density at increasing radius. Since the threshold energy for exciting $O_2(^1\Delta)$ is only 0.98 eV, even electrons having T_e of 0.5–0.6 eV are able to efficiently produce the state [47]. The rate coefficient for electron impact excitation $O_2(^1\Delta)$ in dry air for $T_e = 0.6$ eV (obtained from a stationary solution of the Boltzmann equation) is 1.5×10^{-11} cm^3 s^{-1}. The post-pulse density of N_2^* more closely follows the path of the electron ionization wave as it intersects the N_2 diffusing from the ambient air into the He plume. The minimum threshold energy for creating N_2^* is 6.2 eV. The rate coefficient for electron impact excitation of N_2^* in dry air for $T_e = 0.6$ eV is of 10^{-21} cm^3 s^{-1}, and so there is essentially no direct production of N_2^* by electron impact in the halo. Some of higher excited states of N_2^* radiatively relax and others quench quickly with O_2 to produce O atoms, and with O atoms (when present) to form NO. The lifetime for quenching of N_2^* at the site of its highest density by collisions with O_2 is 1 μs.

The further development of the densities of O and O_3 up to 100 μs after the single discharge pulse is shown in figure 5(a). (This time was chosen as it is the interpulse period for a 10 kHz PRF.) Between 1 and 10 μs, the density of O atoms increases at the tip of the tube through ion–ion recombination between O_2^- and O_2^+. This process is aided by electrons from the plume diffusing radially outward and intersecting the inwardly diffusing O_2 from the air. These low energy electrons then quickly attach to form additional O_2^-. (Although the dynamics of this process likely occur in all plasma jets with a similar geometry, the details of where these additional O atoms are produced are device dependent.) The density of O atoms increases in the channel due to quenching of N_2^* by O_2. This locally high density of O atoms (up to 2×10^{14} cm^{-3} at 10 μs) react with O_2 diffusing from the ambient to form O_3 in nearly the same amount at 100 μs. Between at the end of the discharge pulse, the unreacted O atoms (and additional O

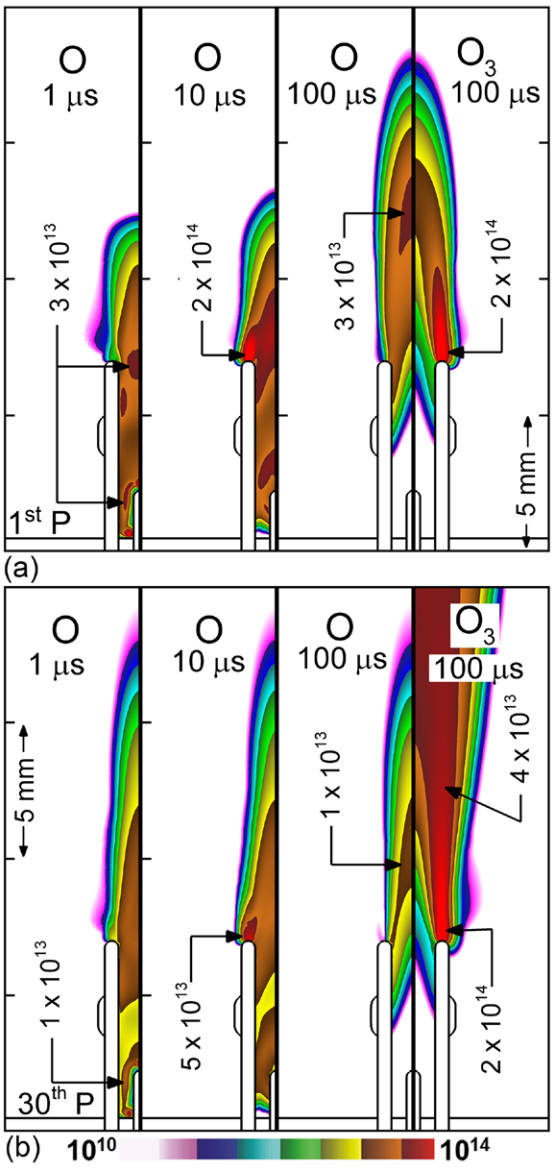

Figure 5. Densities of O and O_3 at different times following the (a) first and (b) 30th discharge pulse at a PRF of 10 kHz. The times selected show the environment that the next pulse would encounter at a 1 MHz, 100 kHz and 10 kHz PRF (left to right). Contours are on a four decade log-scale. At 100 μs, the O atoms produced by the 30th pulse have spread and reacted with O_2 from the ambient to form O_3. The ozone accumulates in the plume.

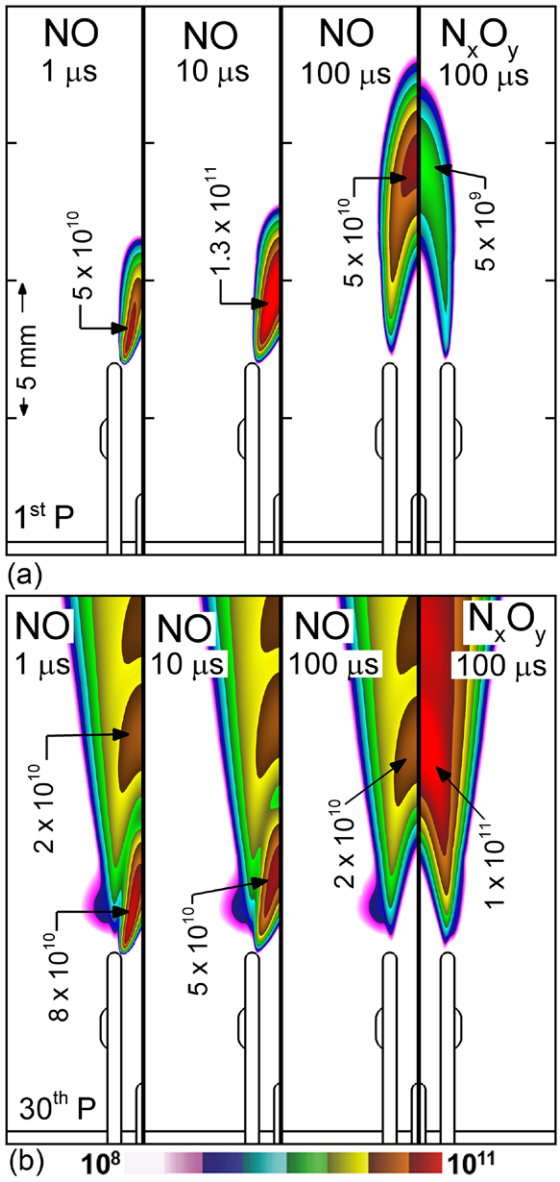

Figure 6. Densities of NO and N_xO_y at different times following the (a) first and (b) 30th discharge pulse at a PRF of 10 kHz. The times selected show the environment that the next pulse would encounter at a 1 MHz, 100 kHz, and 10 kHz PRF (left to right). At a PRF of 10 kHz, the NO produced by the previous pulse(s) moves downstream at lower, but significant, densities. N_xO_y has accumulated to 1×10^{11} cm^{-3} over the 30 pulses in the effluent. Contours are on a three decade log-scale.

atoms produced by quenching of N_2^*) move upward with the flow. The maximum in the density of O atoms translates about 5 mm upward while O atoms are depleted in the tube by this flow. (There are no additional sources of O atoms in the tube after the discharge pulse.) As the O atoms flow upward, they continue to be depleted by formation of O_3.

The formation of NO and N_xO_y (sum of NO_2, NO_3, N_2O_3, N_2O_4 and N_2O_5) up to 100 μs for the first and thirtieth pulse is shown in figure 6. NO is dominantly formed through two, two-step mechanisms. The first is $e + N_2 \rightarrow N + N + e$, followed by $N + O_2 \rightarrow NO + O$. The second is $N_2^* + O \rightarrow NO + N$, which follows production of O atoms. Both of these processes involve reactants requiring high energy electrons in the ionization wave, either to produce N atoms by dissociative excitation of N_2 (threshold energy 11 eV) or to produce N_2^* (minimum threshold energy 6 eV). There is negligible production of N or N_2^* in the halo. Since the lifetime of N_2^* against quenching by O_2 is 1 μs, the second process contributes to NO production only during the first few μs after the discharge pulse. Subsequent production of NO is by the reactions of N atoms with O_2. The production of NO is relatively low (maximum density of 5×10^{10} cm^{-3}) following the single pulse. The low density results from the low production of N atoms (maximum density of 5×10^{11} cm^{-3}), small rate coefficient for the former reaction at the temperature in the effluent

of 300 K (8.1×10^{-17} cm^3 s^{-1}), and short lifetime for N_2^* for the second reaction. Overall, in the first 100 μs, 42% of NO is produced by the reaction of N + O_2 and 58% is produced by the reaction of N_2^* with O. As the gas continues to flow upward, NO is slowly depleted by three-body reactions producing higher oxides. In the near field where O atoms have a higher density, these reactions are NO + O + $M \rightarrow NO_2 + M$ (R31) and NO_2 + O + $M \rightarrow NO_3$ + M (R38). In the far field where the density of O_3 is higher, NO is depleted in the formation of NO_2 (R33) by reaction with O_3. Subsequent reactions of NO_x with O, O_3 and NO_x form higher oxides of nitrogen, N_xO_y (R39), (R42)–(R44).

From the development of the RONS over time shown in figures 5–7, we can envision the environment the next discharge pulse will see in a multiply pulsed system. The densities at 1 μs correspond to the initial conditions for a repetition rate of 1 MHz. For example, at 1 μs, there is still a significant density of O atoms within the tube and near the pin electrode, as shown in figure 5(a). At 10 μs, corresponding to a repetition rate of 100 kHz, the O atoms have moved away from the pin, but are still in the tube. At 100 μs (10 kHz), the O atoms have mostly cleared the tube and are dominantly in the plume. Continuing to lower the PRF will clear out the bulk of the reactive species in the tube and so provide a more pristine environment consisting of the injected gases for the next pulse. A high repetition rate results in the next pulse entering a more reactive environment.

Densities of O and O_3 are shown in figure 5(b) at different times after the 30th discharge pulse for a 10 kHz PRF (100 μs interpulse period). By this pulse, a steady state O atom profile has emerged. Sufficient time has passed (3 ms) for the O atoms to be entrained in the flow extending to about 1.5 cm beyond the tube, and to be consumed by reactions. The dominant reactions which consume O atoms are with O_2 to form O_3, with N_2^* to form NO, and with NO to form NO_2. In the absence of organic compounds and with a low plume gas temperature that slows reactions of O_3 with NO and N_xO_y, O_3 is fairly stable in the plume. In this sense, O_3 is a terminal species and so the density of O_3 accumulates in the effluent up to 4×10^{13} cm^{-3} over the 30 pulses. The major source of O_3 is at the intersection of the O_2 diffusing into the plume and the O atoms flowing up out of the tube in the plume.

The densities of NO and N_xO_y after the 30th discharge pulse are shown in figure 6(b). Since the conversion of NO to N_xO_y is relatively slow (longer than the interpulse period), pulses of NO of 2×10^{10} cm^{-3} convect with the flow. These pulses represent the NO produced in previous pulses as they move vertically upward with the flow. These pulses of NO are slowly depleted, reacting with O, O_3 and NO_x, to form N_xO_y which then accumulates in the plume. After the 30th discharge pulse, the density of N_xO_y accumulating from previous pulses reaches 1×10^{11} cm^{-3}.

The initial formation of the hydroxyl radical, OH, is through electron impact dissociative excitation and ionization of the water vapor diffusing into the plume from the ambient (R9), (R10). Additional sources are dissociative recombination of H_2O^+-(R11) and ion neutralization of O_2^- and H_2O^+-(R12).

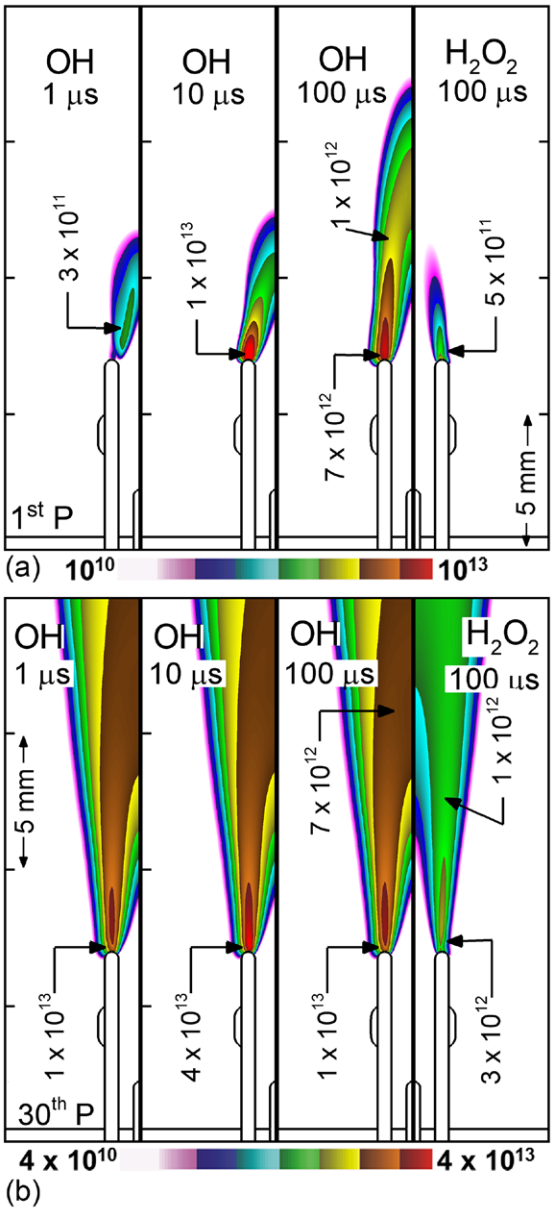

Figure 7. Densities of OH and H_2O_2 at different times following the (a) first and (b) 30th discharge pulse at a PRF of 10 kHz. The times selected show the environment that the next pulse would encounter at a 1 MHz, 100 kHz and 10 kHz PRF (left to right). The OH density is at its maximum at the tip of the dielectric tube at 10 μs, which transitions toward the axis as the humid air diffuses into the helium jet. H_2O_2, primarily created by the reaction of two OH radicals, increases to 1×10^{12} cm^{-3} over the 30 pulses in the effluent following the similar spatial trend of OH. Contours are on a three decade log-scale.

The development of the OH density for the first and thirtieth pulses is shown in figure 7. The production of OH after the first discharge pulse when electron impact dissociation of H_2O terminates is by ion–ion neutralization of the superoxide anion, O_2^-, and H_2O^+ (R12), and electron–ion recombination of H_2O^+ (R11). (This is most clearly illustrated by the 10 and 100 μs frames in figure 7(a).) Hydrogen peroxide is formed by the three-body self-reaction of OH (R13) and

grows appreciably over the 30 pulses. The spatial distribution of H_2O_2 follows that of OH as would be expected. The process of OH and H_2O_2 formation at the end of the dielectric tube is similar that of ozone—relying on diffusion of the ambient air into the active helium plume. The primary rate coefficient for the formation for H_2O_2 by two OH radicals (R13) is larger at ambient temperature than that for formation of ozone by reaction of O and O_2 (R8). However, the higher reactant density favors the development of ozone. As the OH and H_2O_2 convect with and accumulate in the flow, the densities in the effluent are $7 \times 10^{12}\,cm^{-3}$ and $1 \times 10^{12}\,cm^{-3}$, respectively, at the end of the 30th pulse.

IIIb. Voltage

Of the many system variables available to control the production of radicals in the flow, voltage is perhaps the least perturbing to other processes as, in principle, the major effect is the production rates of radicals. We do note that there have been observations of plasma-flow interactions related to voltage that either trigger or delay the onset of turbulence [21], and so our comments here apply to laminar flow.

Densities of electrons, sum of all cations (N^+_{tot}), OH, He*, N^*_2, $O_2(^1\Delta)$ and O are shown in figure 8 at the end of a single discharge pulse for −10,−15,−20 and −30 kV. All voltage pulses have the same rise time (5 ns) and duration (80 ns). These species were chosen as being representative of those produced by direct electron impact or one step removed, as would be the case of charge exchange or Penning reactions. The profiles of densities shown in figure 8 are along the axis. The end of the tube is at an axial location of 0.5 cm. Increasing the applied voltage increases energy deposition which then translates to higher electron densities, but also produces a higher speed of the ionization wave. The speed of the ionization wave increases from $1.2 \times 10^7\,cm\,s^{-1}$ to $4.2 \times 10^7\,cm\,s^{-1}$ from −15 to −30 kV. This higher speed extends the ionized region of the plume to 1.8 cm. The density of N^+_{tot} is predominantly produced from electron impact ionization or one step removed, such as Penning ionization. The densities of all species that are formed in the tube or directly from species formed in the tube first decrease along the axis and then, upon emerging from the tube, increase along the axis. These dynamics result from the ionization wave being initiated on axis at the pin electrode (large density on axis), becoming annular along the wall moving up the tube (low density on axis) and then transitioning back to the axis when emerging from the tube (high density on axis). The densities of OH and N^*_2 first emerge when the ionization wave intersects the ambient air diffusing into the plume beyond the end of the tube, and so these densities do not reflect the radial dynamics of the ionization wave inside the tube.

The densities of O and $O_2(^1\Delta)$ are dominated by electron impact excitation of the initial O_2 in the gas mixture and, upon leaving the tube, O_2 diffusing into the plume from the ambient. Their densities therefore increase and are maximum outside the tube. The production of He* is dominantly by direct electron impact of the ground state (a small contribution comes

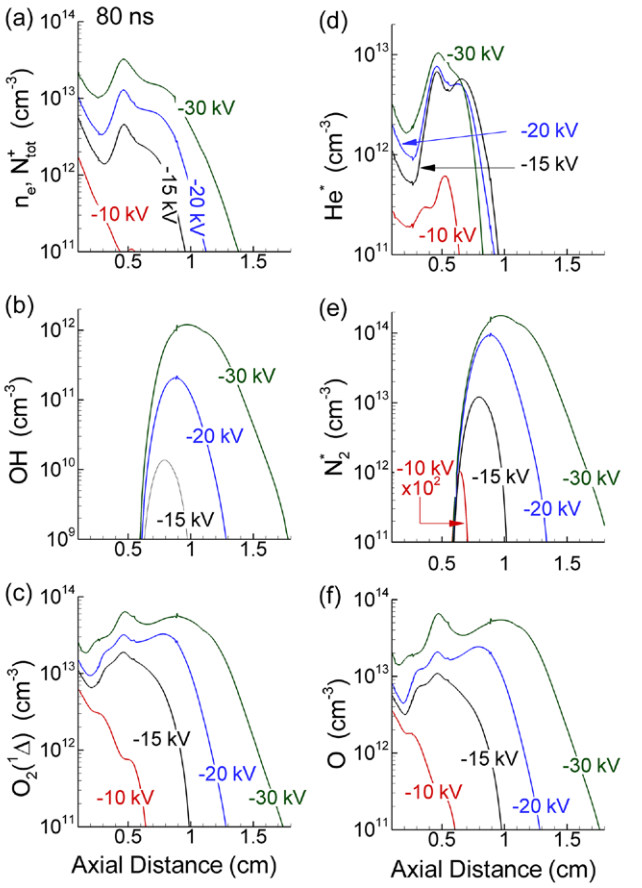

Figure 8. Densities on the axis at the end of the first discharge pulse (80 ns) for voltages of −10 kV,−15 kV (base case),−20 kV and −30 kV. (a) electrons and total cation, (b) OH, (c) $O_2(^1\Delta)$, (d) total He excited states, (e) total N_2 excited states and (f) O atoms. The end of the tube is at 0.5 cm.

from dissociative recombination of He^+_2). Its dominant loss is by Penning reactions with the ambient gases. The density of He* therefore sharply drops upon emerging from the tube when the ambient air begins diffusing into the plume.

The species perhaps most affected by voltage are OH and N^*_2. Without H_2O or N_2 in the initial mixture, OH (dissociative excitation of H_2O) or N^*_2 (direct excitation of N_2) are dominantly produced by intersection of the ionization wave with H_2O and N_2 diffusing into the plume. The excitation energy for the lowest N_2 electronic state is 6.2 eV and so N^*_2 will not be produced in large numbers in the halo. The higher speed and greater penetration distance of the ionization wave with the higher voltage enables the ionization wave to overlap with higher densities of H_2O and N_2 in the plume further from the tube. The fact that He* does not also extend further into the plume with increasing voltage results from the rapid quenching of He* by Penning collisions, and due to its lower rate of production by electron impact resulting from the lower electron temperature in the plume far from the end of the tube. For −30 kV, T_e falls to 2.6 eV a distance of 1 cm from the end of the tube. At this temperature, the electrons are still able to efficiently excite the N_2 (6.2 eV) but do not efficiently excite

He* (19.6 eV). At this point in the discharge, OH is produced from dissociation of the H_2O diffusing into the plume from the ambient.

The significant drop in the density of OH at −10 kV is a demonstration of the influence of the propagation distance of the ionization wave. Significant production of OH requires intersection of the ionization wave with water vapor diffusing into the plume from the ambient. With the lower voltage, the ionization wave simply does not propagate far enough into the plume to intersect with significant densities of H_2O. A similar trend occurs for $O_2(^1\Delta)$. With increasing voltage the ionization wave extends further into the plume where the density of O_2 diffusing from the ambient is larger. The extension of the density of O atoms with voltage is not as great since both its source (ionization wave intersecting with more O_2) and its sink (formation of O_3) both increase further from the tube as the ambient O_2 diffuses into the plume.

The development of RONS (O, O_3, NO, N_xO_y, OH and H_2O_2) after 30 pulses for a PRF of 10 kHz for voltages of −10 to −30 kV are shown in figure 9 to a distance of 4 cm. Densities along the axis are shown in figure 10 for OH, H_2O_2, HNO_x, O_3, NO and N_xO_y for different voltages to a distance of 6 cm. This distance is the extent of the flow after 30 pulses of reactive species that are initially formed in the tube. The increasing rate of formation of O with increasing voltage directly maps onto the increase in the density of O_3. The increasingly more negative voltage also produces a larger halo which also produces more OH, NO, and O_3 at large radius. The nitric oxide acids, HNO_x, shown in figure 10(c) are formed predominantly from the three-body reactions of NO and NO_2 with OH (R49), (R51), (R53). Their axial profile is similar to H_2O_2 indicating the influence of OH in their formation. The axial oscillations in HNO_x result from the axial oscillations in the density of the precursor NO from previous pulses.

Since the gas dynamics (in this model) are not terribly affected by the voltage, the major consequence of voltage on the densities NO and N_xO_y are the increasing densities of precursors. The higher voltages which extend the ionization wave deeper into the plume where N_2 densities are higher produce larger densities of N and N_2^*, the precursors for NO. The periodic maxima of NO densities resulting from prior pulses diminish as the voltage increases. This results from the ionization wave propagating further into the plume, overlapping the prior pulse of NO, and creating more O and OH, that deplete the density of NO.

OH is formed dominantly by electron impact dissociation in the ionization wave of H_2O diffusing into the plume. As the ionization wave penetrates deeper into the plume where the density of H_2O is higher, more OH is produced further from the end of the tube. The ionization wave penetrates to only 2 cm at −30 kV, however the greater extension is preserved by the flow. OH is produced in large numbers mostly by electron dissociative excitation of H_2O in the ionization wave. Reactions between OH to produce H_2O_2, and with NO and N_xO_y to form HNO_x (comprised of HNO_2, HNO_3 and ONOOH) deplete the density OH as the flow extends beyond 2 cm where the OH is dominantly produced. The density of N_xO_y is most sensitive to residence time since forming the higher N_xO_y requires

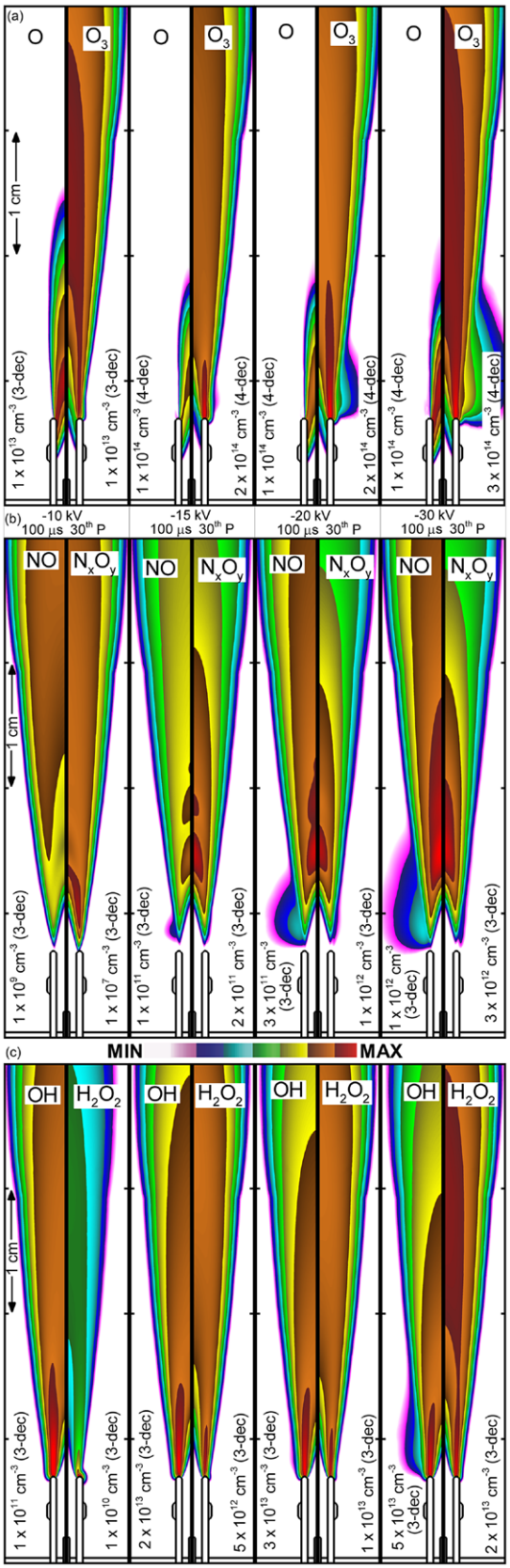

Figure 9. The spatial densities of selected RONS at the end of the 30th pulse for the different voltages (−10 kV,−15 kV,−20 kV,−30 kV). The mixture is He/O_2 = 99.8/0.2 flowing at 4 slm with a 10 kHz PRF. (a) O atoms and O_3. (b) NO and N_xO_y. (c) OH and H_2O_2. Contours are on a log-scale with the number of decades shown in the frame.

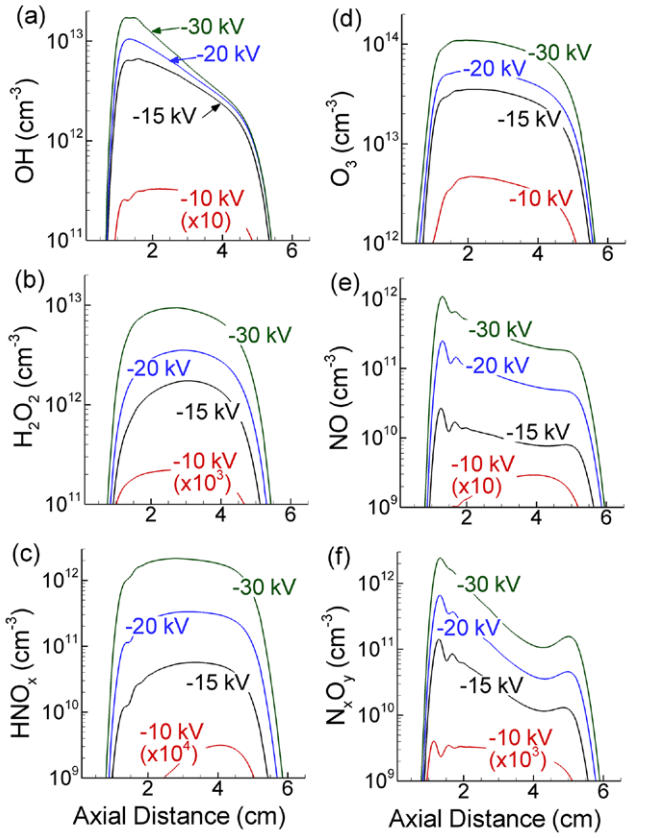

Figure 10. Densities on the axis at the end of 30 pulses for a flow rate of 4 slm for voltages from −10 to −30 kV. (a) OH, (b) H_2O_2, (c) HNO_x, (d) O_3, (e) NO and (f) N_xO_y. The end of the tube is at 0.5 cm. At this flow rate and elapsed time, the reactive species in the effluent reach nearly 5.5 cm from the exit of the tube.

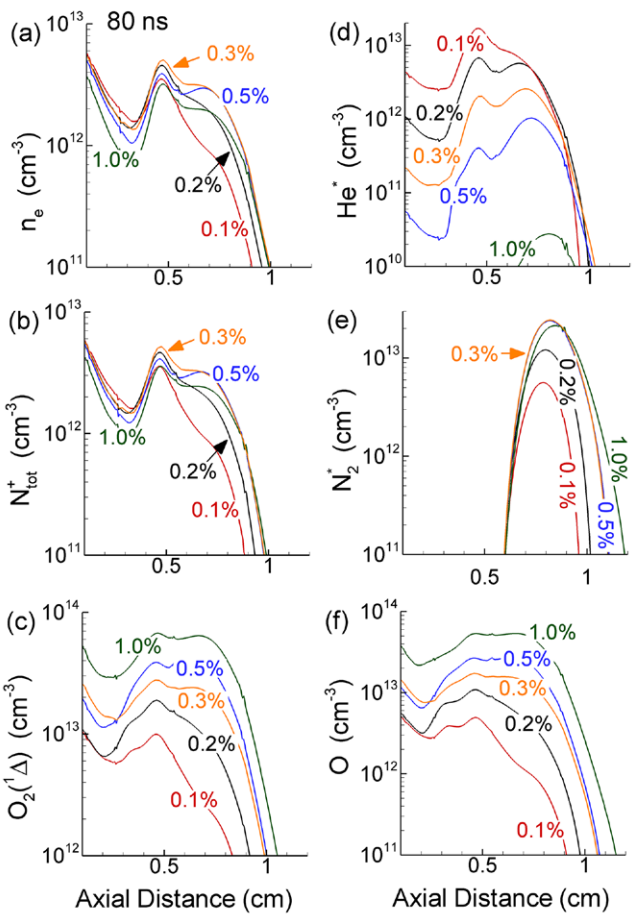

Figure 11. Densities on the axis at the end of the first discharge pulse (80 ns) for O_2 concentrations in He of 0.1%, 0.2% (base case), 0.3%, 0.5%, and 1.0%. (a) electrons, (b) total cation, (c) $O_2(^1\Delta)$, (d) total He excited states, (e) total N_2 excited states and (f) O atoms. The end of the tube is at 0.5 cm.

multiple collisions. (To form N_2O_5, a minimum of 5 collisions are required.) The axial speed decreases with distance from the tube as the plume radially expands. This decrease in axial speed increases the residence time of reactants in the plume which in turn affords more collisions between species, to which N_xO_y is most sensitive. The end result is an increase in N_xO_y at the end of the plume.

IIIc. O_2 fraction in gas feed

The production of specific ROS is sensitive to the fraction of O_2 in the He inlet gases. Experimentally, it was determined that the production of $O_2(^1\Delta)$ was maximum for an O_2 fraction of 0.5% [15] and computational investigations determined that an O_2 fraction of 0.5% maximized O atom production [48]. The densities of electron impact produced species (n_e, N_{tot}^+, $O_2(^1\Delta)$, He*, N_2^* and O) at the end of the first discharge pulse are shown in figure 11 along the axis up to 1.5 cm for O_2 fractions of 0.1% to 1%. In all cases, the increased amount of O_2 in the mixture leads to an increase in the densities of O and $O_2(^1\Delta)$. In spite of O_2 diffusing into the plume, the majority of the oxygen based reactivity is produced by the O_2 flowing through the tube which directly overlaps the ionization wave where the electron density and temperature have their highest values. (Should the plume be turbulent, we expect more O_2 from the ambient would be intersected by the intense portion of the ionization wave.)

The axial electron density inside the tube decreases with increasing O_2 fraction, in large part due to increasing rates of dissociative and three-body attachment to O_2. Outside the tube, the maximum electron density on axis occurs for an O_2 fraction of 0.5%. This result is a bit of an artifact of the dynamics of the ionization wave. Prior to the end of the tube the ionization wave is along the wall of the tube leaving the center of the tube with a lower T_e, which produces less ionization (and on a relative basis, more attachment). When the ionization wave leaves the tube, the maximum rate of ionization returns to the axis. This transition then favors production of ROS for flows with higher O_2 fractions. The density O_2 on axis at this location is most influenced by the initial mole fraction of O_2 and not by diffusion from the ambient.

The density of He* monotonically decreases with increasing O_2 fraction. A portion of this decrease results from the higher rate of quenching of He* by the increasing fraction of O_2 in the feed gas. However with increasing O_2, the electron temperature decreases. For these reasons, the sensitivity of the axial

density of He* to the fraction of O_2 is greater in the tube where the O_2 density on axis is determined by the feed gas than outside the tube where the O_2 density on axis has increasing contributions from the ambient. For example, 3 mm beyond the end of the tube, the maximum T_e decreases from 3.7 eV for an O_2 fraction of 0.1% to 2.3 eV for an O_2 fraction of 1%. This decrease in T_e results in a decrease in the rate coefficient for electron impact excitation of He* from 9×10^{-15} cm^3 s^{-1} for an O_2 fraction of 0.1% to 5×10^{-21} cm^3 s^{-1} for an O_2 fraction of 1%. However, reactions that have lower threshold energies, such as direct electron impact production of N_2^+, O_2^+ and H_2O^+, are less sensitive to the decrease in T_e.

The ionization wave speeds up with increasing O_2 fraction. The speed of the ionization wave is 1×10^7 cm s^{-1} for an O_2 fraction of 0.1% and 1.8×10^7 cm s^{-1} for 1%. This higher speed and greater extension of the ionization wave enables the wave to intersect with higher densities of air diffusing into the plume that produces more N_2^*. Despite the lower value of T_e, the extent of the ionization wave at the end of the pulse for an O_2 fraction of 1% is 3 mm longer than that of the O_2 fraction of 0.1%.

The densities of RONS (O, O_3, NO, N_xO_y, OH, H_2O_2) after 30 pulses are shown figure 12 in the tube and plume for different O_2 fractions. Densities of RONS (OH, H_2O_2, HNO_x, O_3, NO and N_xO_y) along the axis are shown in figure 13. With increasing O_2 fraction, the speed-up and further extension of the ionization wave increases the axial extent of O atom production. When combined with the increase in density of O_2 further from the tube due to diffusion from the ambient, the extended production of O atoms increases the production of ozone, O_3. The higher density and larger spread of O atoms is not only a source of O_3, but also a source of NO. The larger density of O atoms surviving from previous pulses results in N_2^*, and N produced by following pulses to more readily create NO. This accumulation of NO does not directly produce higher densities of N_xO_y. NO accumulates dominantly downstream of the highest concentration of O atoms which are progressively depleted in the plume by formation of O_3 by reactions with the increasing density of O_2. The end result is a decrease in production of NO_2, the dominant N_xO_y species after NO, and precursor for higher N_xO_y.

The axial density of OH is significantly higher for O_2 mole fractions of 0.1% and 0.2%, as shown in figure 13(a), These trends result, in part, from higher rates of production of H_2O^+ produced by Penning ionization facilitated the larger densities of He*. The larger density of H_2O^+ produces OH by dissociative electron–ion recombination and by ion–ion neutralization with O_2^- (R11), (R12). The higher densities of OH then react with other hydroxyl radicals in three-body collisions to form H_2O_2 and with NO_x to form HNO_x.

After 30 pulses at a PRF of 10 kHz, the inventories of selected terminal or near-terminal species (O_3, NO, N_xO_y, OH, H_2O_2, and HNO_x) are shown in figure 14. The inventory is the spatial integral of the species over the entire computational domain. The inventories are perhaps a better indication of total reactivity produced by the plume than the density at selected locations. The integrated inventory of ozone is not a very sensitive function of O_2 mole fraction with only

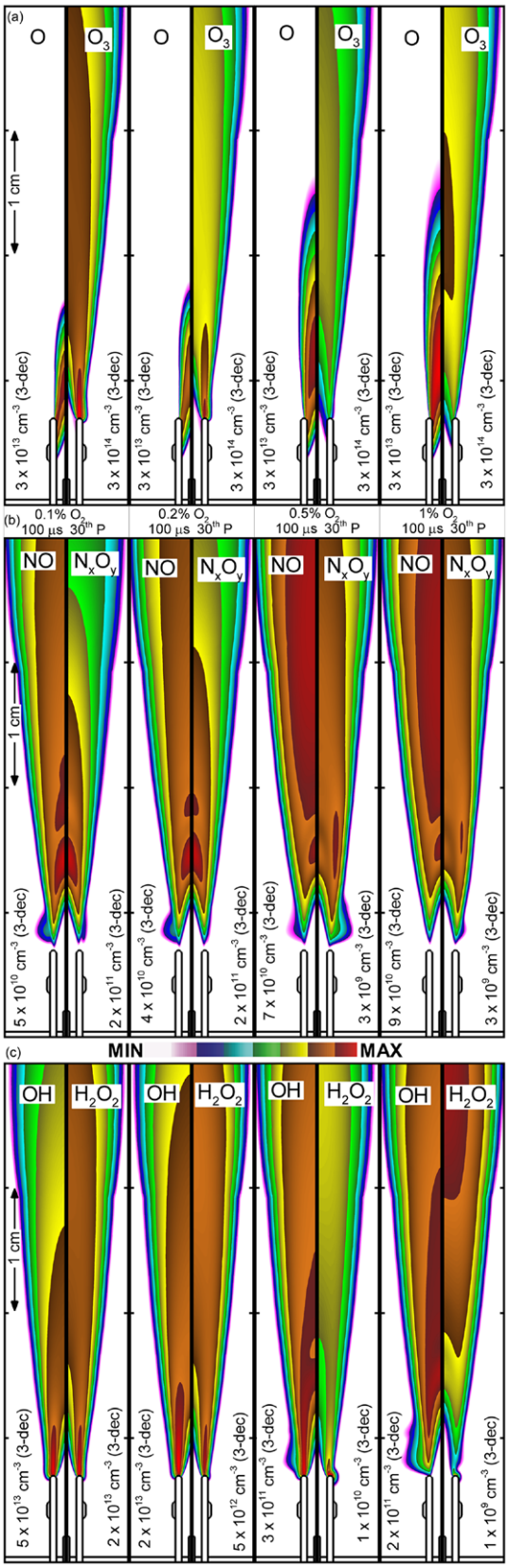

Figure 12. The densities of selected RONS at the end of the 30th pulse for O_2 concentration in He of 0.1%, 0.2%, 0.5% and 1.0% O_2. The conditions are −15 kV pulse, flow of 4 slm and PRF of 10 kHz. (a) O atoms and O_3. (b) NO and N_xO_y. (c) OH and H_2O_2. Contours are on a three decade log-scale.

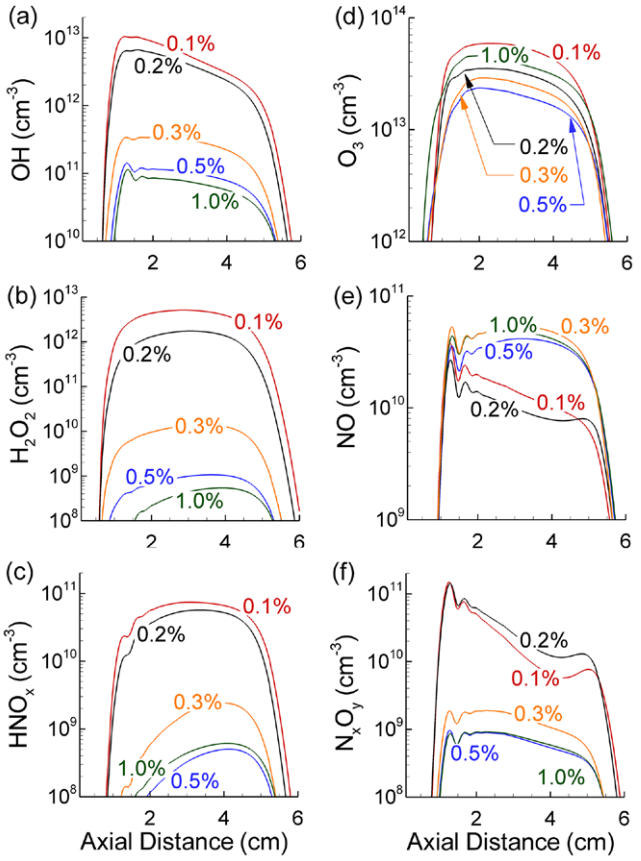

Figure 13. Densities on the axis at the end of the 30th discharge pulse for O_2 concentrations in He of 0.1%, 0.2% (base case), 0.3%, 0.5% and 1.0%. (a) OH, (b) H_2O_2, (c) HNO_x, (d) O_3, (e) NO and (f) N_xO_y.

a reduction of 50% from the mole fraction with the highest inventory (0.1%) and to smallest inventory least (0.5%). The higher inventories of N_xO_y produced for the 0.1% and 0.2% O_2 fractions indicate that the NO is produced in the proper spatial location to react with O atoms and ozone to form NO_2, (R31), (R33) which then leads to N_xO_y (R38), (R39), (R42)–(R44). The higher spatial concentration of O_3 near the axis and the higher concentrations of N_xO_y are also shown for 0.1% and 0.2% fractions of O_2 in figure 12. The trends of higher densities of OH and H_2O_2 on the axis produced with small fractions of O_2 (0.1% and 0.2%) extend to the total inventory as well. An order of magnitude higher inventory of OH is produced with 0.1% and 0.2% fractions of O_2 ($(3–4) \times 10^{12}$) compared to 0.3% (3×10^{11}). This higher inventory of OH at relevant spatial locations to react with NO and N_xO_y produces the significantly higher inventory HNO_x (R49), (R51) and (R53). Increasing O_2 mole (1–2%) can significantly decrease RONS species with the exception of O_3 and $O_2(^1\Delta)$. Although more O atoms are produced at the end of the discharge pulse, the higher mole fraction of O_2 quickly scavenges the O in the formation of O_3, and so fewer O atoms remain for other reactions. Depending on the desired treatment outcome, the fraction of oxygen can be used to vary the relative fractions of RONS. For example, small mole fractions of O_2 produce

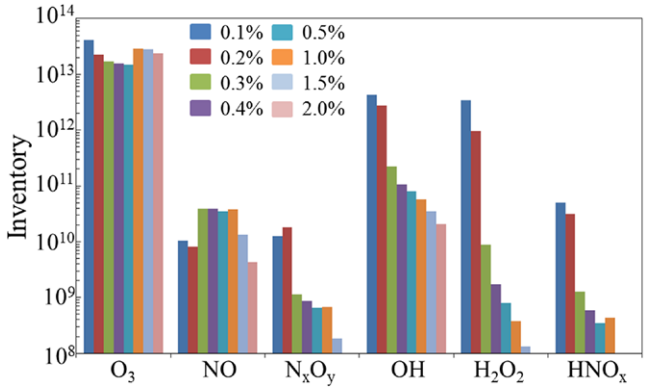

Figure 14. The inventory (spatial integral) of selected species at the end of the 30th discharge pulse for O_2 concentrations from 0.1% to 2%. The O_3 inventory is relatively constant. The lower inventory of NO for 0.1% and 0.2% can be attributed to the higher amount of N_xO_y at the end of the 30th pulse. The NO is depleted by reactions with O to form NO_2.

larger densities of OH, H_2O_2 and HNO_x relative to O_3 than obtained at large mole fractions of O_2. Intermediate fractions of O_2 increase the ratio of NO/O_3.

IIId. Flow

Changing the flow rate has direct consequences on the flow dynamics. The flow speed increases which, for a constant PRF, decreases the residence time of species in the tube and extends the plume where the He mole fraction is large. As the flow rate of the He/O_2 mixture increases the diffusion of humid air into the helium jet begins further from the exit of the tube. In spite of these changes in flow dynamics, at the end of the first pulse, there is little change in the discharge for flow rates of 2–7 slm since the speed of the ionization wave is much higher than that of the gas. However, when varying flow rate, significant differences occur in the densities of RONS at 100 μs after the pulse. (Recall that 100 μs is the interpulse period for a 10 kHz pulse PRF.) Densities of RONS on the axis for flow rates of 2, 3, 5 and 7 slm are shown in figure 15 at 100 μs after the pulse. For a flow rate of 2 slm, the ROS formed in the tube (O, $O_2(^1\Delta)$ and O_3) have not flowed out of the tube by the time of the next discharge pulse. For these ROS there are two maxima—in the tube resulting from in-tube production of ROS that has not yet flowed out of the tube, and outside the tube where the ionization wave has intersected O_2 diffusing into the plume. At the higher flowrates of 4, 5 and 7 slm, the higher flow speed carries the ROS out of the tube and into the effluent prior to the next pulse.

The integral rate of production of RONS by electron impact processes (on the first pulse) is not a sensitive function of flow rate while the speed of the flow increases. So in the absence of other processes a pulse of reactants would flow downstream with increasing speeds into increasing densities of diffusing air. For terminal species such as $O_2(^1\Delta)$, its *plug* of density largely translates further downstream with increasing flow rate with a peak axial density of 2.3×10^{13} cm^{-3} that changes by less than 30% with flow rate. O_3 and OH, which benefit from the greater mixing with the ambient humid air that occurs with

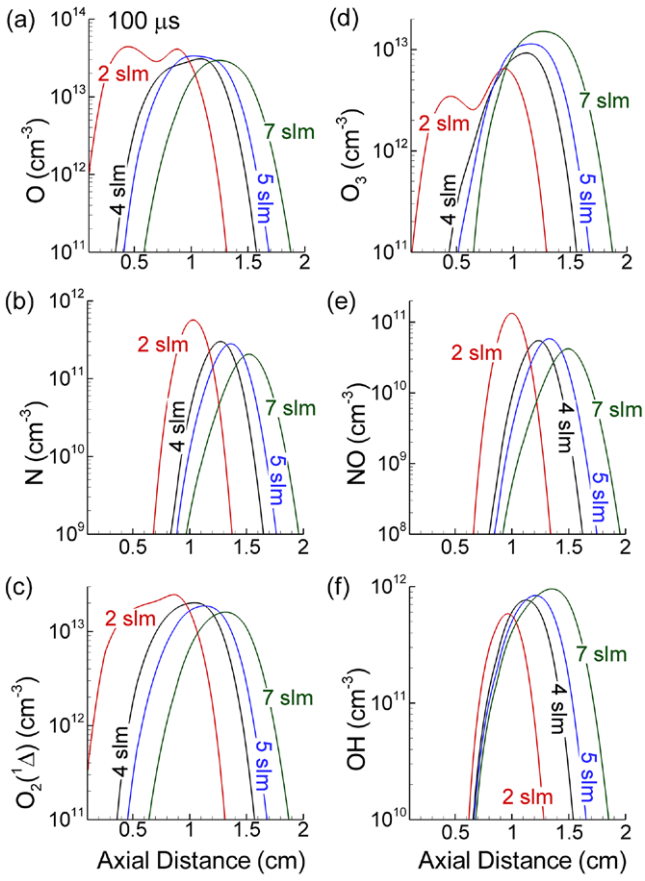

Figure 15. Axial densities for flow rates of 2 slm, 4 slm (base case), 5 slm and 7 slm 100 μs after the of the discharge pulse. (a) O, (b) N, (c) $O_2(^1\Delta)$, (d) O_3, (e) NO and (f) OH. The end of the tube is at 0.5 cm.

the longer plume, have densities that increase with flow rate. The minor decrease in the maximum axial densities of N and NO with increasing flowrate after 100 μs is a bit deceiving as the total inventory of N and NO is approximately the same. The N and NO are initially produced over a larger spatial extent because the ionization wave penetrates further from the tube through the extended portion of the plume having a large He mole fraction.

The PRF and flow rate collectively determine the environment that a successive discharge pulse encounters. For a PRF of 10 kHz and a flow of 7 slm, the next pulse will enter a pristine environment since the RONS formed on the previous pulse has largely flowed out of the tube. For a flow rate of 2 slm, the discharge will encounter the RONS still in the tube formed during the previous pulse. The densities of O, O_3, NO, N_xO_y, OH and H_2O_2 after 30 pulses are shown in figure 16 for flow rates of 2–7 slm. Densities of RONS (OH, H_2O_2, HNO_x, O_3, NO and N_xO_y) along the axis for these conditions are shown in figure 17. The density of O_3 in the effluent 3 cm from the inlet is maximum with the 2 slm flow rate (4.3×10^{13} cm^{-3}) and a minimum with the 7 slm flow rate (2.3×10^{13} cm^{-3}). The spatial integral (inventory) of O_3 produced over 30 pulses increases from 1.9×10^{13} molecules for a flowrate of 2 slm to 3.9×10^{13} molecules for a flowrate of 7 slm. This increase in

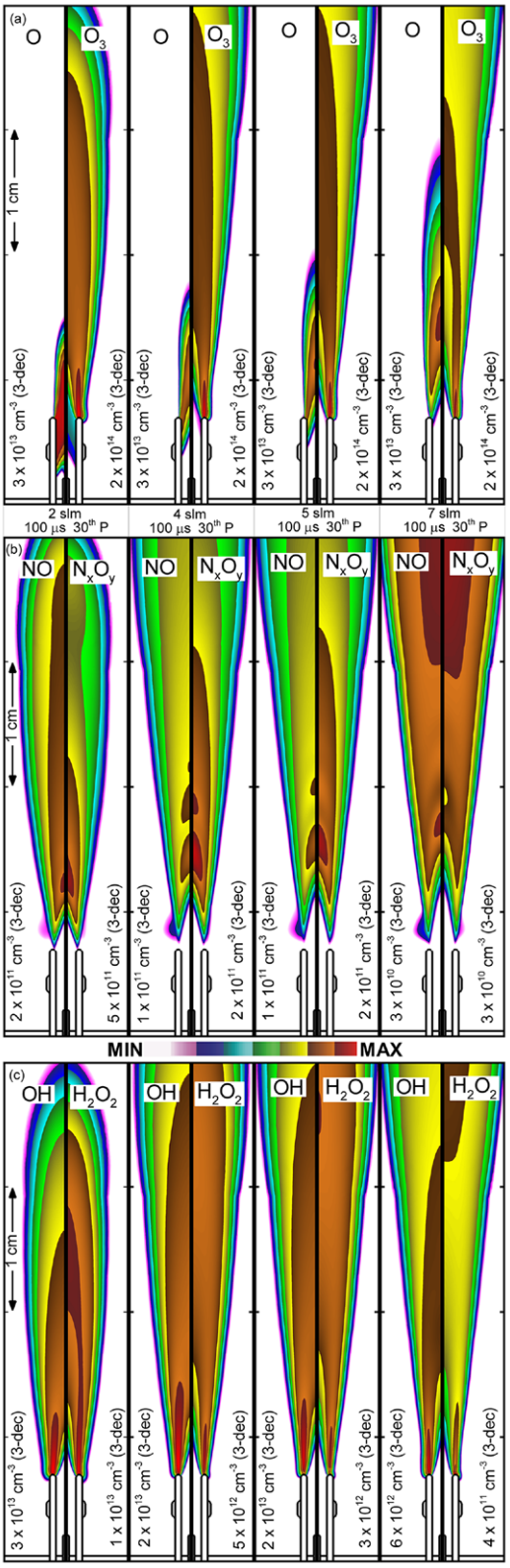

Figure 16. Densities of RONS at the end of the 30th discharge pulse for flow rates of 2–7 slm with −15 kV pulses at 10 kHz and $He/O_2 = 99.8/0.2$ (a) O and O_3, (b) NO and N_xO_y, (c) OH and H_2O_2. At 2 slm, the primary reactants do not flow out of the tube before the next pulse which allows for accumulation. At 7 slm, the primary reactants flow out of the tube and the species formed by the next pulse enter a pristine environment. Contours are on a three decade log-scale from the maximum value listed in the frame.

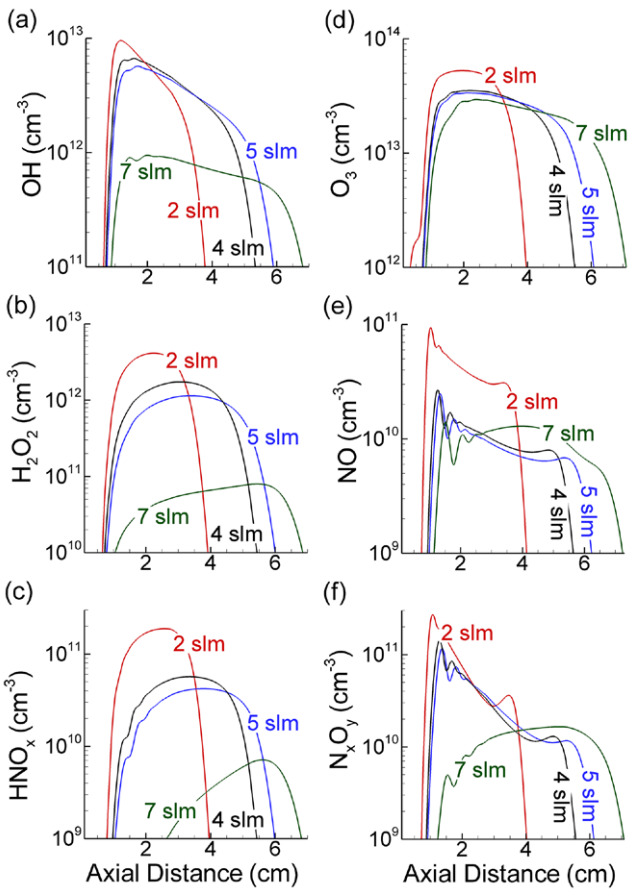

Figure 17. Axial densities for flow rates of 2 slm, 4 slm (base case), 5 slm, and 7 slm at the end of the 30th discharge pulse. (a) OH, (b) H_2O_2, (c) HNO_x, (d) O_3, (e) NO and (f) N_xO_y. The exit of the tube exit is at 0.5 cm.

the inventory of O_3 is enabled by the higher flowrate carrying O atoms further into the plume where they intersect with a higher density of O_2 entering the plume from the ambient. The axial extent of the O_3, a terminal species, increases with flow rate, as observed by Xian *et al* [49]. For a flowrate of 2 slm, the presence of the O atoms in the proximity of the N_2^* produced by the next pulse allows for a large production and accumulation of NO and N_xO_y in the effluent. The higher flow rates transport O atoms further into the effluent away from where N and N_2^* are produced by the ionization wave and so reduces the NO initially formed by subsequent pulses. However, some downstream accumulation of N_xO_y occurs for 7 slm after 3 cm.

The production of O_3 depends nearly linearly on the density of its precursor, O atoms. As a result, its inventory, all other conditions being equal, should not depend strongly on the pulse-to-pulse accumulation of its precursor. Species such as H_2O_2 whose production depends on collisions between a pair of its precursor OH (and so depends on the square of its density) have densities and inventories that are much more sensitive to flow rates. Low flow rates produce more accumulation of OH which translates to a higher inventory of H_2O_2. For example, the inventory of H_2O_2 decreases an order of magnitude from 1.3×10^{12} molecules at 2 slm to 1.3×10^{11} molecules at 7 slm. A similar scaling occurs with production of HNO_x whose density and inventory benefits from the accumulation of its precursors, NO and OH, that occurs at low flow rates.

IIIe. Pulse repetition frequency

PRF is another method of controlling the residence time and accumulation of species between pulses. The length of the interpulse period has significant effects on the density and distribution of the RONS in the effluent of the plasma jet. At high PRFs which produce interpulse periods shorter than the gas clearing time, there is an accumulation of RONS in the plume on a pulse-to-pulse basis, enabling further reactions between these species. At lower PRFs where the interpulse periods are commensurate or longer than the clearing time of the gas through the device, the ionization wave enters a more pristine and controllable environment in which there are fewer reactive species remaining from the prior pulse.

PRF has little effect on the production of primary species during the first pulse, and so our prior discussion on the discharge characteristics of the first pulse for the base case (He/O_2 = 99.8.0.2,−15 kV, 4 slm) in large part applies to all PRF. The PRFs investigated here are 500 kHz, 100 kHz, 50 kHz, 10 kHz and 5 kHz, having interpulse periods of 2 μs, 10 μs, 20 μs, 100 μs and 200 μs. The densities of O and O_3 for a high PRF (100 kHz, 10 μs period) and a low PRF (10 kHz, 100 μs) are shown in figure 18(a) at the end of the 5th and 10th pulses. This corresponds to a total time of 50 μs at the high PRF and 500 μs at the low PRF. The density of O atoms at 100 kHz is nearly an order of magnitude higher than for 10 kHz, a consequence of there being more accumulation between pulses as the O atoms have flowed a shorter distance. In contrast, the inventory of O_3 is significantly higher for the 10 kHz case. The elapsed time for 10 kHz is ten times that for 100 kHz. The longer elapsed time for 10 kHz has enabled flow to extend the plume of O atoms further downstream and to achieve a near steady state profile for O atom density from the 5th to the 10th pulse. The flow of O atoms further downstream intersects with more O_2 diffusing into the plume in addition to the longer time that allows more O atoms to react to form O_3.

Densities of O and O_3 are shown in figure 18(b) at the end of the 30th pulse for PRFs of 500 kHz, 100 kHz, 50 kHz and 10 kHz (corresponding to elapsed times of 60 μs, 0.3 ms, 0.6 ms and 3 ms). Since energy deposition per pulse is essentially the same, examining densities after the same number of pulses compares results after the same energy deposition. After 30 pulses at the highest PRF of 500 kHz, O atoms have accumulated in the tube and in the effluent with a maximum density of 5×10^{14} cm^{-3} as the interpulse period is shorter than the gas clearing time. The O atoms have not yet been converted to O_3 due to both the shorter elapsed time and since the plume of O atoms has not yet encountered the high density of O_2 that occurs further downstream where diffusion of ambient air into the jet occurs. As the PRF decreases for the same number of pulses (and essentially the same production of O atoms), the O atom density first increases and then reduces its extent and value. At 100 kHz the plume of O atoms is 2 cm long and the density is above 10^{14} cm^{-3}. At 10 kHz the O atom

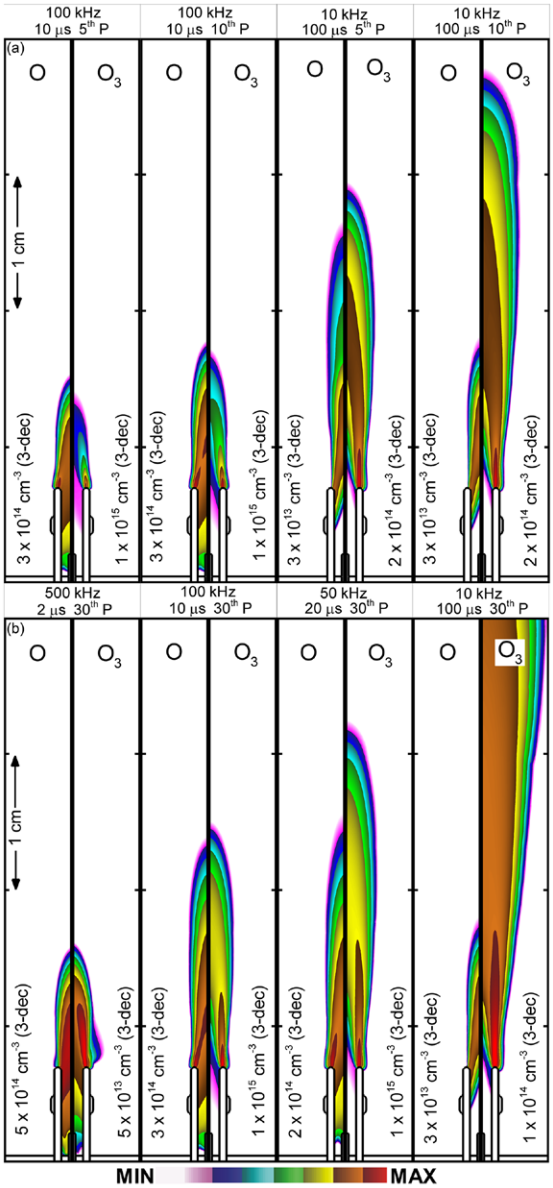

Figure 18. O atom and O_3 densities for −15 kV, 4 slm and He/O_2 = 99.9/0.2. (a) Densities at the end of 5th and 10th discharge pulses for 100 kHz (left) and 10 kHz (right) PRF. The higher PRF allows O atoms to accumulate in the tube. (b) Densities at the end of the 30th discharge pulse for PRFs of 500 kHz to 10 kHz. Note the accumulation of O atoms in the tube in the high PRF cases. The O_3 plume is longer, though less dense for the low PRF cases. Contours are on a three decade log-scale from the maximum value listed on the frame.

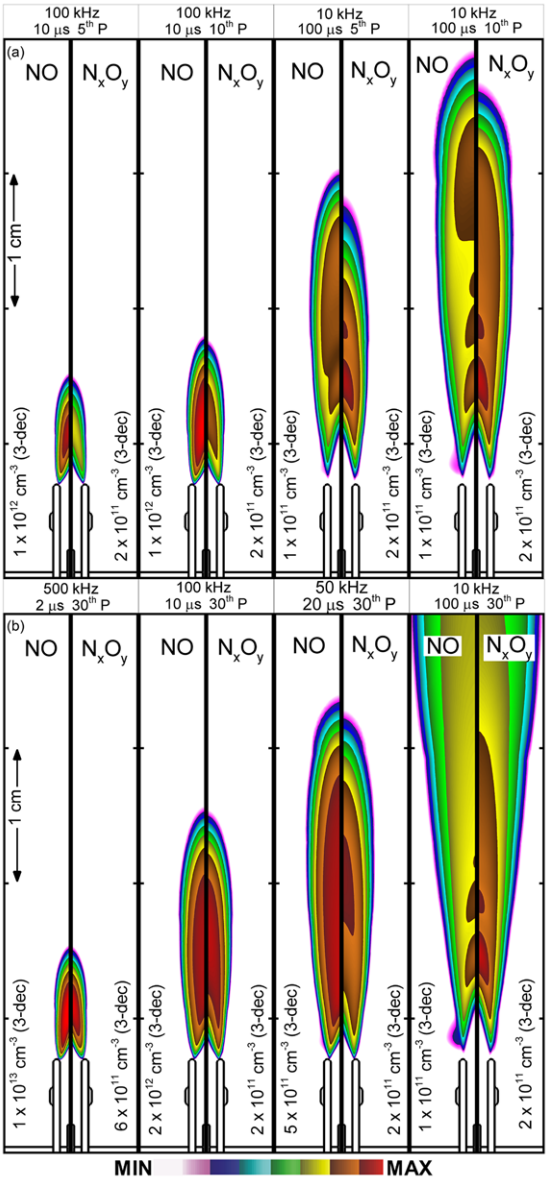

Figure 19. NO atom and N_xO_y densities for −15 kV, 4 slm and He/O_2 = 99.9/0.2. (a) Densities at the end of 5th and 10th pulses for 100 kHz (left) and 10 kHz (right) PRF. (b) Densities at the end of the 30th discharge pulse for PRFs of 500 to 10 kHz. The higher PRF allows NO to accumulate in the tube. For the lower PRFs, NO accumulates at lower densities further downstream. The NO accumulation is significant in the high PRF cases. Contours are on a three decade log-scale with the maximum value noted in each frame.

density is 10^{12} cm^{-3} the plume is only 1 cm at the onset of the next pulse. The plume of the ozone extends beyond that for the O atom at 100 kHz and the length of the O_3 plume continues to increase with lower PRF (longer elapsed time). The diminishing density of O atoms in the plume at low PRF (long elapsed time) compared to high PRF is due, in part to the reaction of O atoms with NO, N_xO_y and H_2O formed during the longer elapsed time.

The densities of NO and N_xO_y for a high PRF (100 kHz, 10 μs period) and a low PRF (10 kHz, 100 μs) are shown in figure 19(a) at the end of the 5th and 10th pulses. Densities are shown in figure 19(b) at the end of the 30th pulse for PRFs of 500 kHz, 100 kHz, 50 kHz and 10 kHz. Operating at the higher PRF enables more accumulation of NO on a pulse-to-pulse basis prior to the gas flowing downstream. The density of NO is 10^{12} cm^{-3} after 10 pulses at 100 kHz and 10^{13} cm^{-3} after 30 pulses at 500 kHz. As O atoms enter this environment and react with NO, N_xO_y increases to 2×10^{11} cm^{-3} after only 10 pulses. At the other extreme, lower PRFs allow for the NO created during the pulse to move with the flow further from the active plasma, a location where there would be opportunity for reacting with O to form N_xO_y. The longer

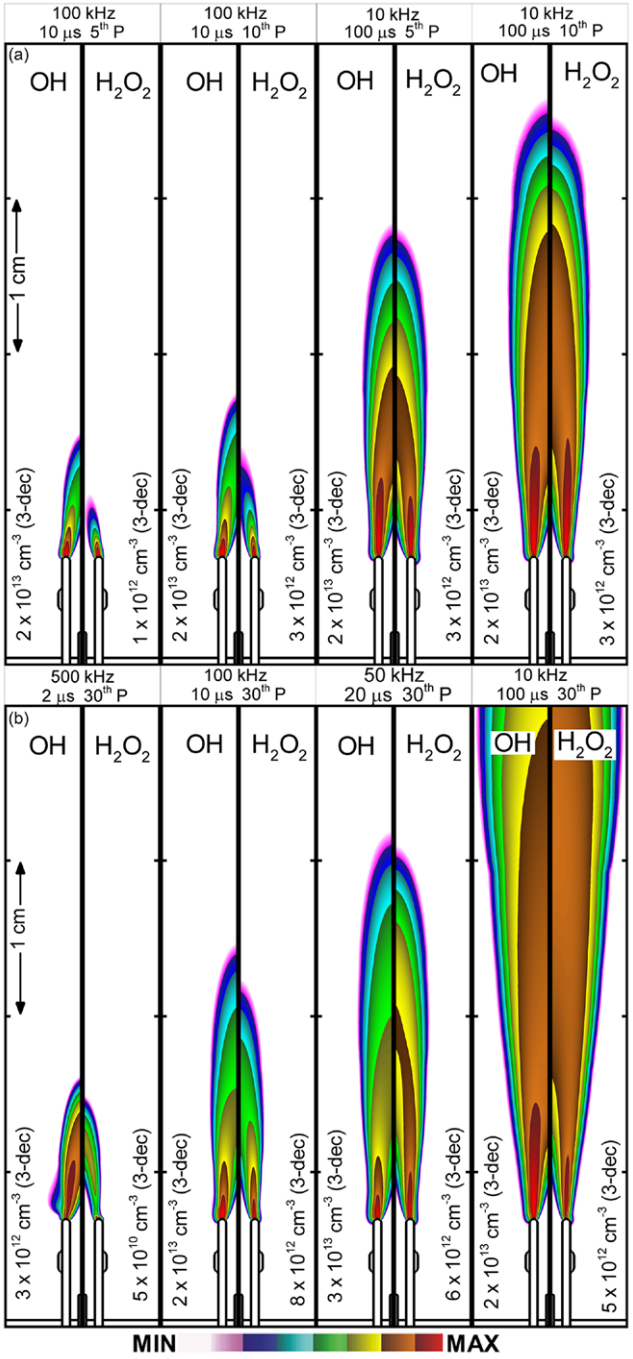

Figure 20. OH and H_2O_2 densities for −15 kV, 4 slm and He/O_2 = 99.9/0.2. (a) Densities at the end of the 5th and 10th pulses for 100 kHz (left) and 10 kHz (right) PRF. (b) Densities at the end of the 30th discharge pulse for PRFs of 500 kHz to 10 kHz. Contours are on a three decade log-scale with the maximum value noted in each frame.

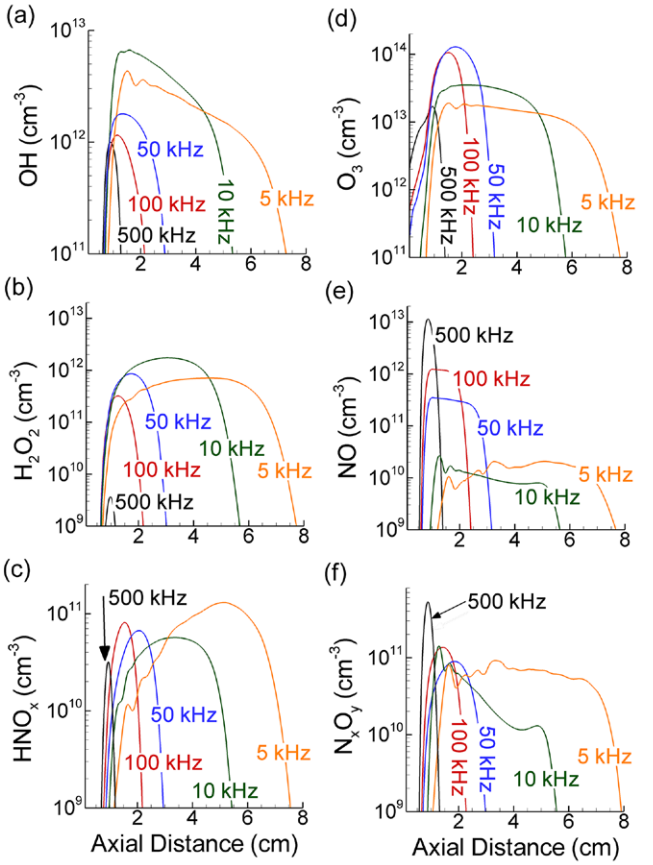

Figure 21. Axial densities for PRFs of 500, 100, 50, 10 and 5 kHz at the end of their 30th discharge pulse. (a) OH, (b) H_2O_2, (c) HNO_x, (d) O_3, (e) NO and (f) N_xO_y. The end of the tube is at 0.5 cm. The length of the effluent is proportional to the total elapsed time after the 30 pulses at the different PRFs.

interpulse periods also tend to preserve the pulses of NO and N_xO_y formed from the previous pulses, visible in the plumes for 10 kHz. At 5 kHz (not shown), the pulses begin to merge as there is sufficient time for diffusion and mixing with the ambient gases to blur the boundaries

The NO is highly concentrated at high PRF (500 kHz) with densities exceeding 10^{13} cm^{-3} and corresponding densities of N_xO_y of 5×10^{11} cm^{-3}. As the PRF decreases to 100 kHz, the plume spreads while densities drop to 10^{12} and 10^{11} cm^{-3} for NO and N_xO_y. As the PRF decreases, the peaks of density from previous pulses have flowed downstream and the accumulation of RNS tends to occur more downstream where the axial speed decreases.

The densities of OH and H_2O_2 for a high PRF (100 kHz, 10 μs period) and a low PRF (10 kHz, 100 μs period) are shown in figure 20(a) at the end of the 5th and 10th pulses. Densities at the end of the 30th pulse are shown in figure 20(b) for all PRFs. The growth in the density of OH begins at the edge of the dielectric tube at the boundary between the inflowing ambient air and the ionization wave. The maximum density of OH is 2×10^{13} cm^{-3} at this boundary and grows toward the axis (100 kHz PRF) or onto the axis (10 kHz) with subsequent pulses.

The densities on the axis up to 8 cm after 30 pulses for OH, H_2O_2, HNO_x, O_3, NO and N_xO_y are shown in figure 21 for PRFs of 5 to 500 kHz. The accumulation of the terminal species O_3, H_2O_2 and HNO_x extends along the axis for the low PRF cases due to the longer residence times. Maximum densities of OH and H_2O_2 in the effluent occurs at 10 kHz with peak values of 7×10^{12} cm^{-3} and 2×10^{12} cm^{-3},

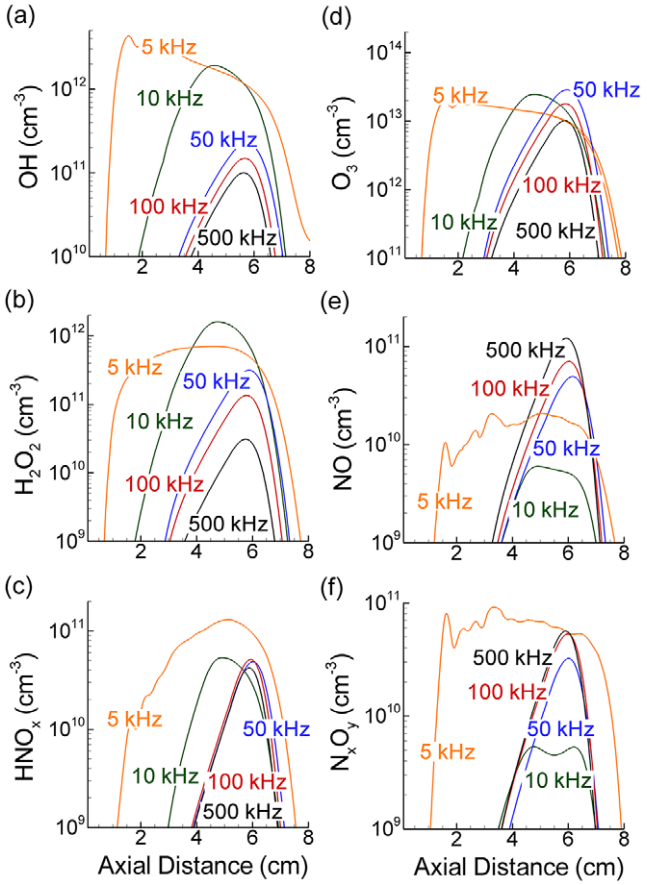

Figure 22. Axial densities for PRFs of 500, 100, 50, 10 and 5 kHz after a total elapsed time of 6 ms (corresponding to the end of the 30th pulse at 5 kHz PRF case). In each case 30 pulses were computed, followed by flow without additional pulsing until a total time of 6 ms. (a) OH, (b) H_2O_2, (c) HNO_x, (d) O_3, (e) NO and (f) N_xO_y. The end of the tube is at 0.5 cm.

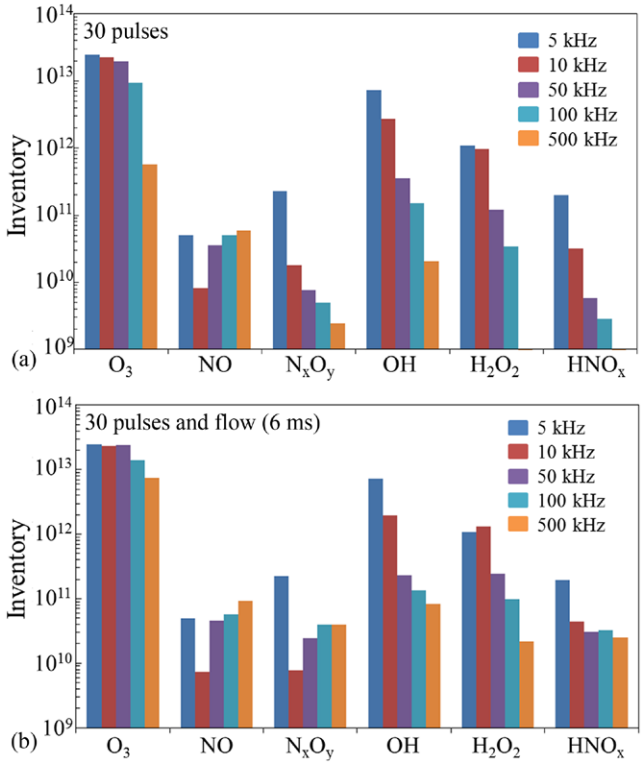

Figure 23. Total inventory (integral of the density over the entire volume) for different PRF. (a) Inventory immediately after the completion of the 30th pulse. (b) Inventory after 30 pulses followed by additional flow for the same elapsed time of 6 ms. The additional flow time allows for the creation of O_3, H_2O_2, N_xO_y and HNO_x in the 50, 100 and 500 kHz cases.

respectively. The limited axial extent of the radicals after 30 pulses at 500 kHz (short residence time) leads to lower concentrations of OH and H_2O_2. The higher PRFs produce locally high densities of O and NO that then facilitate locally higher densities of HNO_x and N_xO_y. At these flow rates and for this geometry, the long interpulse period at the lower PRFs allows RONS formed in the tube to flow out into the plume.

The discussion of densities as a function of PRF for the same number of pulses (and same energy deposition) is complicated by the different elapsed times. To minimize the consequences of elapsed time, densities along the axis are shown in figure 22 for different PRFs for a total elapsed time of 6 ms. This elapsed time coincides with the completion of the 30th pulse at 5 kHz. For higher PRFs, 30 pulsed discharge periods were simulated followed additional time for flow and chemistry until a total elapsed time of 6 ms. For example, this additional flow time is 5.7 ms for the 100 kHz case. The additional flow time after 30 pulses for all PRFs other than 5 kHz results in a *plug* of reactants flowing downstream. After 30 pulses (shown in figure 21), the higher PRFs, 500 and 100 kHz, produce the highest densities of NO and the lowest densities of OH and H_2O_2. All PRFs produce similar densities of O_3 with a reduction in the peak density from 3×10^{13} cm^{-3} at 50 kHz to 1×10^{13} cm^{-3} at 500 kHz. The higher density of ozone in the 5 kHz case spread over six cm in the effluent and its proximity to the large spatial extent of NO and NO_2 lead to the greater production of N_xO_y.

The total inventories of O_3, NO, N_xO_y, OH, H_2O_2, and HNO_x at the end of the 30th pulse are shown in figure 23(a) for different PRF. Inventories at the end of 30 pulses with additional flow to 6 ms are shown in figure 23(b). High repetition rates result in the next pulse entering a more reactive environment. The subsequent discharge pulses will increase the possibility of quenching, recombination or reaction of RONS directly produced by the ionization wave (or once removed such as Penning reactions) with the reactants from the prior pulse. This phenomenon assists the production of N_xO_y and hinders the production of OH, H_2O_2 and HNO_x. Terminal RONS which depend linearly on their precursors, such as O_3, have lower inventories at higher PRF after a fixed number of pulses due to the shorter elapsed time. These inventories rebound to be commensurate with lower PRF after flowing for the same total time. RONS that depend on multiple collisions, such as N_xO_y have inventories that decrease with increasing PRF for a fixed number of pulses due to the shorter reaction time. The inventories increase with increasing PRF after the same flow time. This reversal in the magnitude of the inventory, favoring high PRF, results from

the greater spatial overlap between the precursors at high PRF compared to low PRF. (Recall that for high PRF, the plug of overlapping precursors propagates downstream together.) The increase in the inventory for HNO_x with increasing PRF results from the same spatial overlap in precursor densities. The high inventory of NO for the 5 kHz case appears to be an artifact of having the elapsed time coincide with the end of its 30th pulse.

IV. Concluding remarks

In this computational investigation, production of RONS in an oxygen seeded He plasma jet flowing into atmospheric pressure humid air was discussed for different voltage, flow rate, repetition rate and O_2 admixture. Several trends emerged in the analysis of the development of RONS over 30 discharge pulses. The first is the importance of residence time on the reaction hierarchy. Low flow rate and high PRF results in RONS produced on a previous pulse remaining in the discharge tube and near the exit of the tube. (High flow rates and low PRF result in short residence times and the RONS flowing out of the tube.) RONS produced by a subsequent pulse then accumulates, which enables more reactions that produce higher order RONS that require multiple reactions, such as N_xO_y and HNO_x. A second trend is that over a range of mole fractions, less oxygen in the initial mixture increases the inventory of RONS produced over 30 discharge pulses. This is in part due to a more intense ionization wave that propagates deeper into the plume into which ambient air is diffusing, A third trend is that although higher voltages do deposit more energy, a significant effect of increasing voltage is that the faster, more intense ionization wave penetrates further into the plume. This creates more reactive species in the near field of a longer effluent that react to form the quasi-terminal species, O_3, H_2O_2, N_xO_y and HNO_x in greater quantities in the far field. Lastly, the total elapsed time is important. A comparison of the inventories of RONS for different PRFs at the end of the 30th pulse and after the same elapsed time shows that the additional time allows for reactions between species that are in spatial proximity. The higher densities of reactants that accumulate at high PRF flows downstream together and mutually react. The additional flow time increased the overall inventory of RONS requiring multiple reactions for the high PRF cases, such as HNO_x and N_xO_y.

Acknowledgments

This work was supported by the Department of Energy Office of Fusion Energy Science (DE-SC0001319) and the National Science Foundation (CHE-1124724).

References

[1] Schutze A, Jeong J, Babayan S, Park J, Selwyn G and Hicks R 1998 The atmospheric-pressure plasma jet: a review and comparison to other plasma sources *Trans. Plasma Sci.* **26** 1685

[2] Kong M G, Kroesen G, Morfill G, Nosenko T, Shimizu T, van Dijk J and Zimmerman J L 2009 Plasma medicine: an introductory review *New J. Phys.* **11** 115012

[3] Laroussi M 2009 Low-temperature plasmas for medicine? *Trans. Plasma Sci.* **37** 714

[4] Laroussi M, Kong M, Morfill G and Stolz W 2012 *Plasma Medicine: Applications of Low-Temperature Gas Plasmas in Medicine and Biology* (Cambridge: Cambridge University Press) pp 1–6

[5] Keidar M, Shashurin A, Volotskova O, Stepp M, Srinivasan P, Sandler A and Trink B 2013 Cold atmospheric plasma in cancer therapy *Phys. Plasmas* **20** 057101

[6] Teschke M, Kedzierski J, Finantu-Dinu E G, Korzec D and Engemann J 2005 High-speed photographs of a dielectric barrier atmospheric pressure plasma jet *Trans. Plasma Sci.* **33** 310

[7] Kong M G, Ganguly B N and Hicks R F 2012 Plasma jets and plasma bullets *Plasma Sources Sci. Technol.* **21** 030201

[8] Tian W and Kushner M 2014 Atmospheric pressure dielectric barrier discharges interacting with liquid covered tissue *J. Phys. D: Appl. Phys.* **47** 165201

[9] Lu X, Laroussi M and Puech V 2012 On atmospheric-pressure non-equilibrium plasma jets and plasma bullets *Plasma Sources Sci. Technol.* **21** 034005

[10] Kogelshatz U 2013 Dielectric-barrier discharges: their history, discharge physics, and industrial applications *Plasma Chem. Plasma Proc.* **23** 1

[11] Kossyi I, Kostinsky A, Matveyev A and Silakov V 1992 Kinetic scheme of non-equilibrium discharge in nitrogen-oxygen mixtures *Plasma Sources Sci. Technol.* **1**

[12] Fridman A, Chirokov A and Gutsol A 2005 Non-thermal atmospheric pressure discharges *J. Phys. D: Appl. Phys.* **38** 21

[13] Lu X, Jiang Z, Xiong Q, Tang Z, Hu X and Pan Y 2008 An 11 cm long atmospheric pressure cold plasma plume for applications of plasma medicine *Appl. Phys. Lett.* **92** 081502

[14] Graves D B 2012 The emerging role of reactive oxygen and nitrogen species in redox biology and some implications for plasma applications to medicine and biology *J. Phys. D: Appl. Phys.* **45** 263001

[15] Sousa J S, Niemi K, Cox L J, Th Algwari Q, Gans T and O'Connell V 2011 Cold atmospheric pressure plasma jets as sources of singlet delta oxygen for biomedical applications *J. Appl. Phys.* **109** 123302

[16] Reuter S, Tresp H, Wende K, Hammer M, Winter J, Masur K, Schmidt-Bleker A and Weltmann K-D 2012 From RONS to ROS: tailoring plasma jet treatment of skin cells *Trans. Plasma Sci.* **40** 2986

[17] Reuter S, Winter J, Schmidt-Bleker V, Tresp H, Hammer M and Weltmann K-D 2012 Controlling the ambient air affected reactive species composition in the effluent of an argon plasma jet *Trans. Plasma Sci.* **40** 2788

[18] Karakas E, Akman M and Laroussi M 2012 The evolution of atmospheric-pressure low-temperature plasma jets: jet current measurements *Plasma Sources Sci. Technol.* **21** 034016

[19] Walsh J L and Kong M G 2008 Frequency effects of plasma bullets in atmospheric glow discharges *Trans. Plasma Sci.* **36** 954

[20] Lu X, Naidis G V, Laroussi M and Ostrikov K 2014 Guided ionization waves: theory and experiments *Phys. Rep.* **540** 123

[21] Robert E, Sarron V, Darny T, Ries D, Dozias S, Fontane J, Joly L and J-M Pouvesle 2014 Rare gas flow structuration in plasma jet experiments *Plasma Sources Sci. Technol.* **23** 012003

[22] Lay B, Moss R, Rauf S and Kushner M 2003 Breakdown processes in metal halide lamps *Plasma Sources Sci. Technol.* **12** 8
[23] Xiong Z and Kushner M J 2010 Surface corona-bar discharges for production of pre-ionizing UV light for pulsed high-pressure plasmas *J. Phys. D: Appl. Phys.* **43** 505204
[24] Scharfetter D and Gummel H 1969 Large-signal analysis of a silicon read diode oscillator *IEEE Trans. Electron Devices* **16** 1
[25] Liu D, Bruggeman P, Iza F, Rong M and Kong M 2010 Global model of low-temperature atmospheric-pressure He + H_2O plasmas *Plasma Sources Sci. Technol.* **19** 025018
[26] Murakami T, Niemi K, Gans T, O'Connell D and Graham W 2013 Comparison of a global model to semi-kinetic fluid simulations for atmospheric pressure radio-frequency plasmas *Plasma Sources Sci. Technol.* **22** 032001
[27] Dorai R 2002 *PhD Thesis* Department of Chemical Engineering, University of Illinois at Urbana-Champaign
[28] Sakiyama Y, Graves D B, Chang H-W, Shimizu T and Morfill G 2012 Plasma chemistry model of surface microdischarge in humid air and dynamics of reactive neutral species *J. Phys. D: Appl. Phys.* **45** 425201
[29] Van Gaens W and Bogaerts A 2013 Kinetic modelling for an atmospheric pressure argon plasma jet in humid air *J. Phys. D: Appl. Phys.* **46** 275201
[30] Niemi K, Waskoenig J, Sadeghi N, Gans T and O'Connell D 2011 The role of helium metastable states in radio-frequency driven helium–oxygen atmospheric pressure plasma jets: measurement and numerical simulation *Plasma Sources Sci. Technol.* **20** 0550055
[31] Phelps A V 1985 Tabulations of collision cross sections and calculated transport and reaction coefficients for electron collisions with O_2 *JILA Information Center Report No 28*
[32] Popov N A 2011 Fast gas heating in a nitrogen-oxygen discharge plasma: I. Kinetic mechanism *J. Phys. D: Appl. Phys.* **44** 285201
[33] NIST Chemical Kinetics Database, Standard Reference Database 17, Version 7.0 (Web Version), Release 1.6.8 Data Version 2013.03 (http://kinetics.nist.gov/kinetics/index.jsp)
[34] Itikawa Y 2005 Cross sections for electron collisions with water molecules *J. Phys. Chem. Ref. Data* **34** 1
[35] Rowe B R, Vallee F, Queffelec J L, Gomet J C and Morlais M 1988 The yield of oxygen and hydrogen atoms through dissociative recombination of H_2O^+ ions with electrons *J. Phys. Chem.* **88** 845
[36] Itikawa Y, Hayashi M, Ichimura A, Onda K, Sakimoto K, Takayanagi K, Nakamura M, Nishimura H and Takayanagi T 1986 Cross sections for collisions of electrons and photons with nitrogen molecules *J. Phys. Chem. Ref. Data* **15** 985
[37] Uddi M, Jiang N, Adamovich I and Lempert W 2009 Nitric oxide density measurements in air and air/fuel nanosecond pulse discharges by laser induced fluorescence *J. Phys. D: Appl. Phys.* **42** 075205
[38] Shkurenkov I, Burnette D, Lempert W and Adamovich I 2014 Kinetics of excited states and radicals in a nanosecond pulse discharge and afterglow in nitrogen and air *Plasma Sources Sci. Technol.* **23** 065003
[39] Person J C and Ham D O 1988 Removal of SO_2 and NO_x from stack gases by electron beam irradiation *Radiat. Phys. Chem.* **31** 1
[40] Walsh J and Kong M 2008 Contrasting characteristics of linear-field and cross-field atmospheric plasma jets *Appl. Phys. Lett.* **93** 111501
[41] Bogey C and Bailly C 2010 *Direct and Large-Eddy Simulation VII: Proc. 7th Int. ERCOFTAC Workshop on Direct and Large Scale Eddy Simulation VII* (Springer Science) ed V Armenio *et al*
[42] Jiang C, Chen M T and Gundersen M A 2009 Polarity-induced asymmetric effects of nanosecond pulsed plasma jets *J. Phys. D: Appl. Phys.* **42** 232002
[43] Naidis G V 2011 Simulation of streamers propagating along helium jets in ambient air: polarity-induced effects *Appl. Phys. Lett.* **98** 141501
[44] Babaeva N Y and Kushner M J 2014 Interaction of multiple atmospheric-pressure micro-plasma jets in small arrays: He/O_2 into humid air *Plasma Sources Sci. Technol.* **23** 015007
[45] Hoentsch M, von Woedtke T, Weltmann K-D and Nebe J B 2012 Time-dependent effects of low-temperature atmospheric-pressure argon plasma on epithelial cell attachment, viability and tight junction formation *in vitro* *J. Phys. D: Appl. Phys.* **45** 025206
[46] Breden D and Raja L L 2014 Computational study of the interaction of cold atmospheric helium plasma jets with surfaces *Plasma Sources Sci. Technol.* **23** 065020
[47] Hon J, Hager G, Helms C and Truesdell K 1996 Heuristic method for evaluating COIL performance *AIAA J.* **34** 1595
[48] Lee H W, Park G Y, Seo Y S, Im Y H, Shim S B and Lee H J 2011 Modelling of atmospheric pressure plasmas for biomedical applications *J. Phys. D: Appl. Phys.* **44** 053001
[49] Xian Y, Lu X, Wu S, Chu P and Pan Y 2012 Are all atmospheric pressure cold plasma jets electrically driven? *Appl. Phys. Lett.* **100** 123702